

# A thermodynamic model for di-trioctahedral chlorite from experimental and natural data in the system $\text{MgO-FeO-Al}_2\text{O}_3\text{-SiO}_2\text{-H}_2\text{O}$ : applications to $P$ - $T$ sections and geothermometry

Pierre Lanari · Thomas Wagner · Olivier Vidal

Received: 19 August 2013 / Accepted: 10 January 2014  
© Springer-Verlag Berlin Heidelberg 2014

**Abstract** We present a new thermodynamic activity-composition model for di-trioctahedral chlorite in the system  $\text{FeO-MgO-Al}_2\text{O}_3\text{-SiO}_2\text{-H}_2\text{O}$  that is based on the Holland–Powell internally consistent thermodynamic data set. The model is formulated in terms of four linearly independent end-members, which are amesite, clinocllore, daphnite and sudoite. These account for the most important crystal-chemical substitutions in chlorite, the Fe–Mg, Tschermak and di-trioctahedral substitution. The ideal part of end-member activities is modeled with a mixing-on-site formalism, and non-ideality is described by a macroscopic symmetric (regular) formalism. The symmetric interaction parameters were calibrated using a set of 271 published chlorite analyses for which robust independent temperature estimates are available. In addition, adjustment of the standard state thermodynamic properties of sudoite was required to accurately reproduce experimental brackets involving sudoite. This new model was tested by

calculating representative  $P$ - $T$  sections for metasediments at low temperatures ( $<400$  °C), in particular sudoite and chlorite bearing metapelites from Crete. Comparison between the calculated mineral assemblages and field data shows that the new model is able to predict the coexistence of chlorite and sudoite at low metamorphic temperatures. The predicted lower limit of the chloritoid stability field is also in better agreement with petrological observations. For practical applications to metamorphic and hydrothermal environments, two new semi-empirical chlorite geothermometers named Chl(1) and Chl(2) were calibrated based on the chlorite + quartz + water equilibrium ( $2 \text{ clinocllore} + 3 \text{ sudoite} = 4 \text{ amesite} + 4 \text{ H}_2\text{O} + 7 \text{ quartz}$ ). The Chl(1) thermometer requires knowledge of the  $(\text{Fe}^{3+}/\Sigma\text{Fe})$  ratio in chlorite and predicts correct temperatures for a range of redox conditions. The Chl(2) geothermometer which assumes that all iron in chlorite is ferrous has been applied to partially recrystallized detrital chlorite from the Zone houillère in the French Western Alps.

Communicated by T. L. Grove.

**Electronic supplementary material** The online version of this article (doi:10.1007/s00410-014-0968-8) contains supplementary material, which is available to authorized users.

P. Lanari (✉)

Institute of Geological Sciences, University of Bern,  
Baltzerstrasse 1 + 3, 3012 Bern, Switzerland  
e-mail: pierre.lanari@geo.unibe.ch

P. Lanari · O. Vidal

ISTerre, CNRS, University of Grenoble 1, 1381 rue de la  
Piscine, 38041 Grenoble, France

T. Wagner

Division of Geology, Department of Geosciences and  
Geography, University of Helsinki, Gustaf Hållströmin katu 2a,  
00014 Helsinki, Finland

**Keywords** Thermodynamics · Chlorite · Sudoite · Geothermometry · Solid solution ·  $P$ - $T$  section

## Introduction

Chlorite minerals are commonly observed in diverse geological settings including sedimentary, metamorphic and hydrothermally altered rocks. This common rock-forming mineral occurs within pelitic, mafic, ultramafic and calc-silicate assemblages, resulting in a large compositional variability. In addition, the chemical composition of chlorite in hydrothermal alteration zones changes systematically with proximity to fluid pathways and hydrothermal veins and it can be used for reconstructing the fluid

composition (Walshe 1986; Mountain and Williams-Jones 1995; Halter et al. 1998). Chlorite can occur as replacement of preexisting minerals such as biotite that control its chemical composition via local dissolution–reprecipitation reactions. Conversely, chlorite can directly grow as newly formed metamorphic or diagenetic phase, with a composition dictated by the bulk rock composition and mineral equilibria (Lanari et al. 2012). It is now well established that the chemical composition of chlorite does also depend on the conditions of formation such as temperature and pressure and can be used for thermobarometric estimates in various geological contexts (Cathelineau and Nieva 1985; Walshe 1986; Kranidiotis and MacLean 1987; Cathelineau 1988; Hillier and Velde 1991; Jowett 1991; de Caritat et al. 1993; Zang and Fyfe 1995; Baker and Holland 1996; Vidal and Parra 2000; Vidal et al. 2001, 2006; Le Hébel et al. 2002; Parra et al. 2002b; Árkai et al. 2003; de Andrade et al. 2006; Yamato et al. 2007; Inoue et al. 2009, 2010; Schwartz et al. 2009; Tarantola et al. 2009; Plissart et al. 2009; Saravanan et al. 2009; Verlaquet et al. 2011; Ganne et al. 2012; Grosch et al. 2012; Lacroix et al. 2012; Lanari et al. 2012; Bourdelle et al. 2013a, b; Pourteau et al. 2013; Cantarero et al. 2013; Lanari et al. 2013b). During the last 30 years, three different approaches to chlorite thermometry were developed:

1. Empirical thermometers based on the amount of tetrahedral aluminum ( $Al_{IV}$ ) or on the amount of octahedral vacancies ( $\square$ ) of chlorite (Cathelineau and Nieva 1985; Kranidiotis and MacLean 1987; Cathelineau 1988; Hillier and Velde 1991; Jowett 1991; Zang and Fyfe 1995).
2. Semi-empirical thermometers calibrated using the relationship between temperature ( $1/T$ ) and the equilibrium constant ( $K$ ) of a reaction involving chlorite end-members and typically quartz and water. The equilibrium constant is estimated using ideal mixing of cations on energetically equivalent sites (Walshe 1986; Inoue et al. 2009; Bourdelle et al. 2013a). This assumption of ideal mixing is not compatible with the models used in thermodynamic phase equilibria computation packages (see below), and empirical or semi-empirical calibrations cannot be used in the framework of an internally consistent thermodynamic data set.
3. Following the experiments of Baker and Holland (1996), the mixing properties and activity-composition relationships of chlorite were thermodynamically modeled by Holland et al. (1998). The resulting model, which is termed Chl(HP) for the remainder of the present contribution, was used in equilibrium phase diagram computations such as *THERMOCALC* (Powell et al. 1998; Powell and Holland 2008), *Perple\_X* (Connolly 2005, 2009; Connolly and Pettrini 2002) or *Theriak-Domino* (de Capitani and Petrakakis 2010) in conjunction with the Holland and Powell (1998) internally consistent thermodynamic data set. The solid solution model of Holland et al. (1998) was derived for trioctahedral chlorites, and the composition space was modeled with the four linearly independent end-members Al-free chlorite (afchl), amesite (ames), clinocllore (clin) and daphnite (daph). This model applies for chlorite with an octahedral sum equal to 6 cations based on a formula with 14 anhydrous oxygens and does not account for vacancies in the chlorite structure. However, chlorite in metapelites at low- to medium-grade metamorphic conditions does contain vacancies, which result from the di/trioctahedral substitution toward the sudoite (sud) end-member (Vidal et al. 2001). This precludes the use of the Chl(HP) model at low temperature ( $<450^\circ\text{C}$ ), which is a serious limitation when considering the full temperature range of chlorite stability. The chlorite solid solution models of Vidal et al. (2001, 2005, 2006) include a sudoite end-member. Chlorite compositions are modeled using the amesite, clinocllore, daphnite and sudoite end-members (Vidal et al. 2001) with an extension to Fe–amesite (fames) in updated versions (Vidal et al. 2005, 2006). These models were successfully applied to metapelites using multi-equilibrium techniques (see e.g., Vidal and Parra 2000; Trotet et al. 2001; Parra et al. 2002b; Ganne et al. 2003, 2012; Augier et al. 2005a, b; Vidal et al. 2006; Rimmelé et al. 2006; Yamato et al. 2007; Schwartz et al. 2009; Lacroix et al. 2012; Grosch et al. 2012; Lanari et al. 2012, 2013b; Lanari 2012; Pourteau et al. 2013; Cantarero et al. 2013). However, these models cannot be used for phase diagram computation with the Holland and Powell (1998) internally consistent thermodynamic data set.

Addressing some of the limitations of existing approaches, the purpose of this study is to derive an activity-composition model for chlorite that includes the sudoite end-member and is compatible with the Holland and Powell (1998) internally consistent thermodynamic data set. This model will be constrained from published experimental data on relevant phase equilibria and a set of approximately 270 natural chlorite compositions for which the formation temperature is well constrained. In addition, two semi-empirical geothermometers for chlorite will be derived for the same samples, which cover a much wider range in temperature than previous calibrations. In order to demonstrate the performance of the new chlorite activity-composition model, we show several application examples that include  $P$ – $T$  section

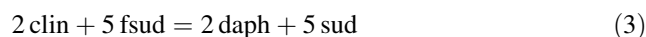
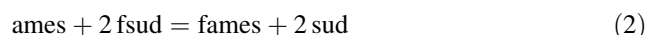
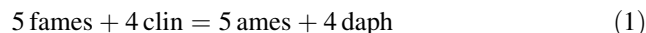
modeling and geothermometry using small-scale microprobe X-ray imaging.

### A new thermodynamic model for chlorite: Chl(LWV)

The chlorite solid solution model of Holland et al. (1998) considered the Fe–Mg<sub>–1</sub> substitution (FM), the Tschermak substitution (TK) Al<sub>IV</sub>Al<sub>VI</sub>Si<sub>–1</sub>(Mg,Fe)<sub>–1</sub> and possible order–disorder along the join between amesite and Al-free chlorite. Restricting our analysis to chlorite with Si < 3, these substitutions can be modeled with the four end-members clinocllore, daphnite, Mg–amesite and Fe–amesite. The extended solid solution model considers the possible incorporation of octahedral vacancies (□) resulting from the di-trioctahedral substitution (DT) (Mg,Fe<sup>2+</sup>)<sub>3</sub>□<sub>–1</sub>Al<sub>–2</sub>, between the above trioctahedral end-

members and the di-trioctahedral end-members sudoite and Fe–sudoite (fsud).

The extended solid solution model, named Chl(LWV) in the following sections, involves thus six end-members (Table 1; Fig. 1a). From this full set of end-members, three internal reactions can be written (see Fig. 1b–d, respectively):



Two of these reactions are linearly independent, and two end-members in the selected set are compositionally dependent, provided that the proportions of some end-members in the independent set can become negative. For phase equilibria computation using common petrological software packages, the thermodynamic properties of the dependent end-members are not required. However, generic nonlinear Gibbs energy minimization codes such as GEM-Selektor (Wagner et al. 2012; Kulik et al. 2013) that find the amount and composition of stable phases by applying a set of Karush–Kuhn–Tucker conditions (one of these being a nonnegativity constraint) require that the properties of dependent end-members are explicitly defined.

Following the approach of Powell and Holland (1999) and taking ames, clin, daph and sud as linearly independent end-members, the Gibbs free energy of fames and fsud can be derived from the following relationships:

**Table 1** Site partitioning scheme used for the model Chl(LWV)

	T1(2)	T2(2)	M1(1)	M23(4)	M4(1)
Amesite–Mg	Si,Si	Al,Al	Al	Mg,Mg,Mg,Mg	Al
Amesite–Fe*	Si,Si	Al,Al	Al	Fe,Fe,Fe,Fe	Al
Clinocllore	Si,Si	Si,Al	Mg	Mg,Mg,Mg,Mg	Al
Daphnite	Si,Si	Si,Al	Fe	Fe,Fe,Fe,Fe	Al
Sudoite–Mg	Si,Si	Si,Al	□	Mg,Mg,Al,Al	Al
Sudoite–Fe*	Si,Si	Si,Al	□	Fe,Fe,Al,Al	Al

\* Dependent end-members (see text)

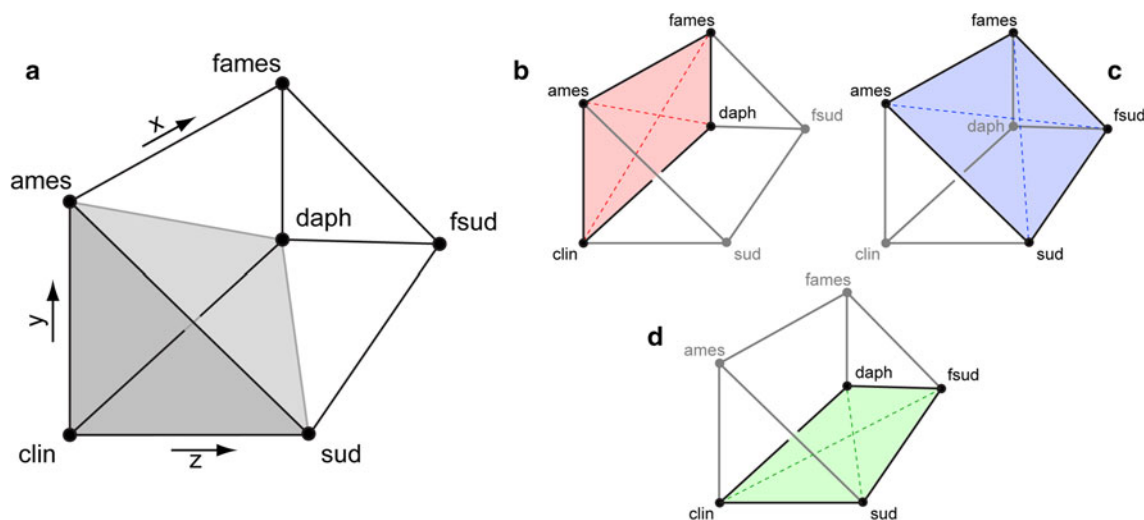


**Fig. 1** Visualization of the chlorite composition space in the system FMASHO. **a** In this model, ames, clin, sud and daph are the independent end-members defining the shaded pyramidal volume (see text). The composition variable  $x$  ( $x = X_{\text{Fe}}$ ) increases from ames to fames (also from sud to fsud and from clin to daph) corresponding to the FeMg<sub>–1</sub> substitution. The composition variable  $y$  ( $y = X_{\text{Al}}^{M1}$ ) increases from clin to ames (also from daph to fames, from sud to

ames and from fsud to fames) corresponding to the TK substitution. The last composition variable  $z$  ( $z = X_{\text{Al}}^{M1}$ ) increases from clin to sud (also from ames to sud, from daph to fsud and from fames to fsud) corresponding to the DT substitution. The internal reactions occur in the three rectangles **b** for the reaction (1), **c** for reaction (2) and **d** for reaction (3) (see text for details)

$$G_{\text{fames}} = G_{\text{ames}} + \frac{4}{5}G_{\text{daph}} - \frac{4}{5}G_{\text{clin}} + \frac{4}{5}W_{\text{ames-clin}} - \frac{16}{25}W_{\text{clin-daph}} \quad (4)$$

$$G_{\text{fsud}} = G_{\text{sud}} + \frac{2}{5}G_{\text{daph}} - \frac{2}{5}G_{\text{clin}} + \frac{2}{5}W_{\text{daph-sud}} - \frac{2}{5}W_{\text{clin-sud}} - \frac{4}{25}W_{\text{clin-daph}} \quad (5)$$

The compositions of the six chlorite end-members can be plotted in a triangular prism showing two triangular faces, with the Mg end-members ames, clin, sud and the Fe end-members fames, daph and fsud, respectively (Fig. 1).

Following common practice to determine the activities of these end-members, the site distribution is formulated in terms of three linearly independent composition variables defined as follows:

$$x = \frac{4X_{\text{fames}} + 5X_{\text{daph}} + 2X_{\text{fsud}}}{4X_{\text{fames}} + 5X_{\text{daph}} + 4X_{\text{ames}} + 5X_{\text{clin}} + 2X_{\text{sud}} + 2X_{\text{fsud}}} = \frac{\text{Fe}}{\text{Fe} + \text{Mg}} = X_{\text{Fe}} \quad (6)$$

$$y = X_{\text{ames}} + X_{\text{fames}} + \frac{1}{2}(X_{\text{clin}} + X_{\text{daph}} + X_{\text{sud}}) = X_{\text{Al,M1}} \quad (7)$$

$$z = X_{\text{sud}} = X_{\text{V,M1}} \quad (8)$$

These three variables account for the compositional variability in the full composition space involving the selected set of chlorite end-members ( $x$ ,  $y$  and  $z$  in Fig. 1a). Assignment of site occupancies followed the approach and the criteria of Vidal et al. (2001). The two tetrahedral T1 sites are fully occupied by Si, and the sites T2 can be occupied by Si and Al. On the octahedral positions, Al preferentially occupies the M4 site, and the remaining amount is distributed over the M1 site and the four M2M3 sites.  $\text{Fe}^{2+}$  and  $\text{Mg}^{2+}$  may occur in M1 and M2M3 sites and are equipartitioned, and  $\square$  is restricted to the M1 site. According to this cation site repartition model, the resulting structural formula of chlorite is then  $(\text{Al})_1(\text{Mg,Fe,Al})_4(\text{Mg,Fe,Al},\square)_1(\text{Si,Al})_2\text{Si}_2\text{O}_{10}(\text{OH})_8$ . For a given composition of chlorite obtained from electron microprobe analysis, the composition variables  $x$ ,  $y$  and  $z$  are evaluated (see details in “Appendix”) to transform the end-member proportions ( $X_{\text{ames}}$ ,  $X_{\text{daph}}$ ,  $X_{\text{clin}}$ ,  $X_{\text{sud}}$ ,  $X_{\text{fames}}$ ,  $X_{\text{fsud}}$ ) into proportions of linearly independent end-members ( $p_{\text{ames}}$ ,  $p_{\text{clin}}$ ,  $p_{\text{daph}}$ ,  $p_{\text{sud}}$ ) with the following equations:

$$p_{\text{ames}} = y \quad (9)$$

$$p_{\text{clin}} = 1 - y - z - x\left(1 - \frac{1}{5}y - \frac{3}{5}z\right) \quad (10)$$

$$p_{\text{daph}} = x\left(1 - \frac{1}{5}y - \frac{3}{5}z\right) \quad (11)$$

$$p_{\text{sud}} = z \quad (12)$$

All chlorite compositions that have nonzero mole fractions of fames or fsud, i.e., those that lie outside the shaded pyramidal volume in Fig. 1a, involve negative proportions of one or more of the independent end-members. The ideal mixing activity of the independent end-members is calculated by on-site mixing of atoms (Powell and Holland 1993). Site fractions are obtained from composition variables as follows:

$$x_{\text{Fe}}^{\text{M23}} = x\left(1 - \frac{1}{2}z\right) \quad (13)$$

$$x_{\text{Mg}}^{\text{M23}} = (1 - x)\left(1 - \frac{1}{2}z\right) \quad (14)$$

$$x_{\text{Al}}^{\text{M23}} = \frac{1}{2}z \quad (15)$$

$$x_{\text{Fe}}^{\text{M1}} = x(1 - y - z) \quad (16)$$

$$x_{\text{Mg}}^{\text{M1}} = (1 - x)(1 - y - z) \quad (17)$$

$$x_{\text{Al}}^{\text{M1}} = y \quad (18)$$

$$x_{\text{Va}}^{\text{M1}} = z \quad (19)$$

$$x_{\text{Al}}^{\text{T2}} = 1 - \frac{1}{2}(1 - y) \quad (20)$$

$$x_{\text{Si}}^{\text{T2}} = \frac{1}{2}(1 - y) \quad (21)$$

The ideal contributions to the activities of independent end-members are then calculated from the site fractions:

$$a_{\text{ames}} = (x_{\text{Mg}}^{\text{M23}})^4 x_{\text{Al}}^{\text{M1}} (x_{\text{Al}}^{\text{T2}})^2 \quad (22)$$

$$a_{\text{clin}} = 4(x_{\text{Mg}}^{\text{M23}})^4 x_{\text{Mg}}^{\text{M1}} x_{\text{Al}}^{\text{T2}} x_{\text{Si}}^{\text{T2}} \quad (23)$$

$$a_{\text{daph}} = 4(x_{\text{Fe}}^{\text{M23}})^4 x_{\text{Fe}}^{\text{M1}} x_{\text{Al}}^{\text{T2}} x_{\text{Si}}^{\text{T2}} \quad (24)$$

$$a_{\text{daph}}^{\text{red}} = 64(x_{\text{Al}}^{\text{M23}})^2 (x_{\text{Mg}}^{\text{M23}})^2 x_{\text{Va}}^{\text{M1}} x_{\text{Al}}^{\text{T2}} x_{\text{Si}}^{\text{T2}} \quad (25)$$

The non-ideal part of the activity ( $\gamma$ ) is expressed using macroscopic activity coefficients (Holland and Powell 1996a, b) and a symmetric formalism:

$$RT \ln(\gamma_{\text{ames}}) = p_{\text{clin}}(1 - p_{\text{ames}})W_{\text{ames-clin}} + p_{\text{daph}}(1 - p_{\text{ames}})W_{\text{ames-daph}} + p_{\text{sud}}(1 - p_{\text{ames}})W_{\text{ames-sud}} - p_{\text{clin}}p_{\text{daph}}W_{\text{clin-daph}} - p_{\text{clin}}p_{\text{sud}}W_{\text{clin-sud}} - p_{\text{daph}}p_{\text{sud}}W_{\text{daph-sud}} \quad (26)$$

$$\begin{aligned}
RT \ln(\gamma_{\text{clin}}) = & p_{\text{ames}}(1 - p_{\text{clin}})W_{\text{ames-clin}} \\
& + p_{\text{daph}}(1 - p_{\text{clin}})W_{\text{clin-daph}} \\
& + p_{\text{sud}}(1 - p_{\text{clin}})W_{\text{clin-sud}} \\
& - p_{\text{ames}}p_{\text{daph}}W_{\text{ames-daph}} - p_{\text{ames}}p_{\text{sud}}W_{\text{ames-sud}} \\
& - p_{\text{daph}}p_{\text{sud}}W_{\text{daph-sud}} \quad (27)
\end{aligned}$$

$$\begin{aligned}
RT \ln(\gamma_{\text{daph}}) = & p_{\text{ames}}(1 - p_{\text{daph}})W_{\text{ames-daph}} \\
& + p_{\text{clin}}(1 - p_{\text{daph}})W_{\text{clin-daph}} \\
& + p_{\text{sud}}(1 - p_{\text{daph}})W_{\text{daph-sud}} \\
& - p_{\text{ames}}p_{\text{clin}}W_{\text{ames-clin}} - p_{\text{ames}}p_{\text{sud}}W_{\text{ames-sud}} \\
& - p_{\text{clin}}p_{\text{sud}}W_{\text{clin-sud}} \quad (28)
\end{aligned}$$

$$\begin{aligned}
RT \ln(\gamma_{\text{sud}}) = & p_{\text{ames}}(1 - p_{\text{sud}})W_{\text{ames-sud}} \\
& + p_{\text{clin}}(1 - p_{\text{sud}})W_{\text{clin-sud}} \\
& + p_{\text{daph}}(1 - p_{\text{sud}})W_{\text{daph-sud}} \\
& - p_{\text{ames}}p_{\text{clin}}W_{\text{ames-clin}} - p_{\text{ames}}p_{\text{daph}}W_{\text{ames-daph}} \\
& - p_{\text{clin}}p_{\text{daph}}W_{\text{clin-daph}} \quad (29)
\end{aligned}$$

where  $W$  are symmetric interaction parameters.

### Model calibration

We apply the following strategy to calibrate the extended chlorite model described above. The initial standard state and symmetric interaction parameters were adopted from Holland and Powell (1998) and subsequent updates (*THERMOCALC* data set file *tcds55*). The standard state properties of Mg-sudoite were refined to bring them into agreement with the available experimental phase equilibria data (Vidal et al. 1992), and the non-ideal interaction parameters describing the mixing of sudoite with the other chlorite end-members were simultaneously refined using natural data from the literature. All computations were performed using *MEAMP* (multi-equilibrium and minimization program), which is a custom developed software tool that allows to plot equilibria in  $P$ - $T$  diagrams and to regress thermodynamic parameters using both experimental and natural data (Lanari 2012).

#### Sudoite molar properties

To preserve consistency with the Holland-Powell thermodynamic data set, the heat capacities, molar volumes, enthalpies, thermal expansion and compressibility parameters of ames, clin and daph were kept unchanged. In the revised data set that was used here (*tcds55*), the entropies of ames, clin and daph were incremented by 20 J/K (Coggon and Holland 2002) compared to Holland and Powell (1998). The equilibrium curve for the reaction Mg-carpholite = Mg-sudoite + quartz + water calculated with the standard state thermodynamic properties from

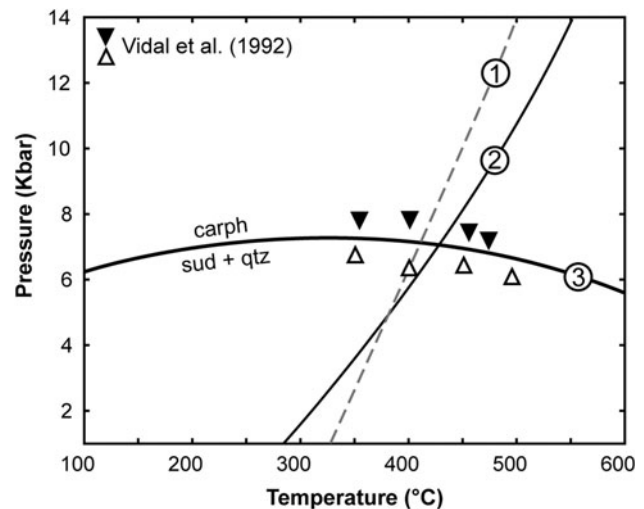


**Fig. 2** Experimental brackets of Vidal et al. (1992) and the model curves of the equilibrium carpholite (carph) = sudoite (sud) + quartz (qtz) plotted using (1) enthalpy, entropy and heat capacity parameters from Holland and Powell (1998), (2) refined enthalpy and entropy with heat capacity parameters from Holland and Powell (1998) and (3) refined enthalpy and entropy and heat capacity parameters (Table 2)

Holland and Powell (1998) (equilibrium 1 in Fig. 2) was found to lie outside of the experimental brackets of Vidal et al. (1992). Considering that the standard state thermodynamic properties of carpholite predict equilibrium curves of other reactions in excellent agreement with the available experimental brackets, it was necessary to refine the properties of Mg-sudoite rather than those of carpholite. A simple adjustment of the enthalpy ( $\Delta_f H^0$ ) and entropy ( $S^0$ ) of Mg-sudoite did not result in better agreement with the experimental constraints, suggesting a problem with the heat capacity ( $C_p$ ) equation for Mg-sudoite proposed by Holland and Powell (1998). Because no calorimetric data are available for Mg-sudoite, the heat capacity coefficients were estimated with the method of Berman and Brown (1985) used in Berman (1988). Figure 3a shows the resulting  $C_p(T)$  function of Mg-sudoite at temperatures ranging from 200 to 600° and compares  $C_p(T)$  with the functions for clin, ames, fames and daph. At any temperature, we note that

$$C_{p_{\text{sud}}}(T_i) < C_{p_{\text{clin}}}(T_i) < C_{p_{\text{ames}}}(T_i) < C_{p_{\text{daph}}}(T_i) \quad (30)$$

The same relative order is observed when plotting the  $C_p(T)$  functions calculated with the Holland-Powell data set, except that the  $C_p(T)$  of sudoite is much higher than that of daphnite (Fig. 3b). Using the predicted heat capacity data and properties from Holland and Powell (1998) as initial guess, the enthalpy ( $\Delta_f H^0$ ), entropy ( $S^0$ ) and heat capacity coefficients of sudoite were simultaneously refined in order to (1) be consistent with Eq. (30), (2) minimize the difference between the refined sudoite



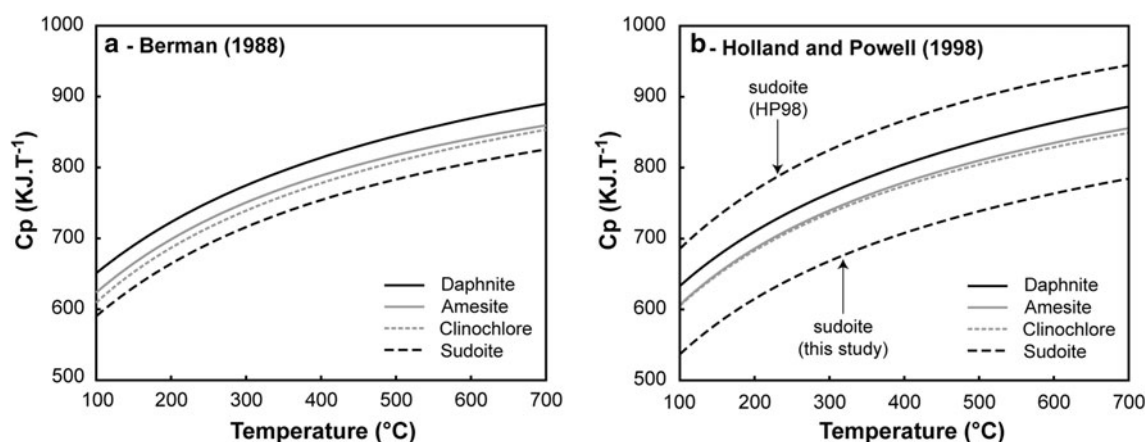


**Fig. 3** Heat capacity of chlorite end-members calculated using **a** the method and coefficients from Berman (1988) and **b** the method and data used in Holland and Powell (1998). The heat capacity curves of

sudoite have been plotted using the data from Holland and Powell (1998) and using the new heat capacity coefficients listed in Table 2

**Table 2** New molar thermodynamic properties (units: kJ, K, bar) of sudoite derived in this study (see text)

	$\Delta_f H$ (kJ)	S (J K <sup>-1</sup> )	V (kJ kbar <sup>-1</sup> )	a (kJ K <sup>-1</sup> )	b (10 <sup>5</sup> ) (kJ K <sup>-2</sup> )	c (kJ K)	d (kJ K <sup>-1/2</sup> )
Sudoite–Mg	–8,647.122	417	20.3	1.1049	1.1217	–6,811.7	–10.1105

$\Delta_f H$  is the enthalpy of formation; S is the entropy; V the volume (all these properties are at 1 bar and 298.15 K)

a, b, c and d are the heat capacity coefficients

standard state properties and those listed in Holland and Powell (1998) and (3) locate the carpholite = sudoite + quartz + water equilibrium within the experimental brackets of Vidal et al. (1992). The resulting parameters are listed in Table 2, the equilibrium curve for the reaction is plotted in Fig. 2 (bold curve, labeled 3), and the  $C_p(T)$  function of Mg–sudoite is plotted in Fig. 3b. The new entropy value for Mg–sudoite derived in the present study differs by 18 kJ compared to that proposed in Holland and Powell (1998), which is consistent with the magnitude of the entropy adjustments to the ames, clin and daph end-members applied by Coggon and Holland (2002) relative to Holland and Powell (1998).

#### Margules parameters on M1

The Fe–Mg mixing on M1 has been accepted to be slightly non-ideal as proposed by Holland et al. (1998), with  $W_{\text{clin-daph}} = 2.5$  kJ. This slight non-ideality is inferred from fluid-mineral Fe–Mg partitioning data (Holland et al. 1998). It is compatible with the assumption of ideal to nearly ideal Fe–Mg mixing made by authors who developed activity-composition models for chlorite (Vidal et al. 2001, 2005, 2006) and dioctahedral mica (Coggon and Holland 2002; Parra et al. 2002a; Dubacq et al. 2009).

The value  $W_{\text{ames-clin}} = 18$  kJ proposed by Holland et al. (1998) was kept unchanged. Similarly, the  $W_{\text{ames-daph}}$  has been fixed to 13.5 kJ, which is the value that is currently

**Table 3** References of the analyses of mineral used for the regression. The reference P–T conditions are plotted in Fig. 4

General range of P–T conditions	References
BT ( $T < 400$ °C)	Cathelineau and Nieva (1985), Zang and Fyfe (1995), Schmidt et al. (1997), Baboury (1999), Vidal et al. (2001), Booth-Rea et al. (2002), Abad et al. (2003), Belmar and Morata (2005), Rolland et al. (2006), Serafimovski et al. (2006), Malasoma and Marroni (2007), Inoue et al. (2009), Shinjoe et al. (2009), Inoue et al. (2010), Lanari et al. (2012), Cantarero et al. (2013)
HT/BP ( $T > 400$ °C $P < 10$ kbar)	Goffé and Bousquet (1997), Hannula et al. (1999), Vidal et al. (1999, 2001), Hoisch (2000), Trotet et al. (2001), Parra et al. (2002b), Moazzen (2004), Augier et al. (2005b), Calderon et al. (2005), Agard et al. (2006), Russo et al. (2006), Inoue et al. (2009)
HP ( $P > 10$ kbar)	Chopin (1979), Goffé and Bousquet (1997), Vidal et al. (1999, 2001), Agard et al. (2001), Parra et al. (2002b), Augier et al. (2005a)

used in *THERMOCALC* in conjunction with the updated mineral standard state data. The small difference between Al–Mg and Al–Fe mixing energies results from the previous assumption of non-ideality in Fe–Mg exchange along the join between clin–daph and ames. The values of the

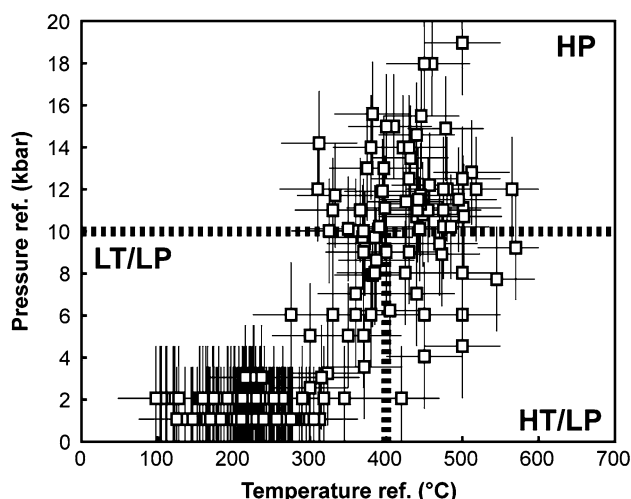


**Fig. 4** Pressure–temperature conditions of the natural data used for regressing the interaction parameters involving sudoite. References for all data sources are given in Table 3

interaction parameters involving sudoite ( $W_{\text{ames-sud}}$ ,  $W_{\text{clin-sud}}$  and  $W_{\text{daph-sud}}$ ) were simultaneously refined by using a set of natural chlorite compositional data in conjunction with published equilibrium conditions ( $P_{\text{ref}}$ ,  $T_{\text{ref}}$ ) in the range of 100–600 °C and 1–20 kbar (see list of references in Table 3 and the  $P$ – $T$  plot in Fig. 4). The compositional variables  $x$ ,  $y$  and  $z$  (Eqs. 6, 7 and 8) were calculated from the chlorite structural formulae (“Appendix”). Analyses with very small amounts of sudoite ( $z < 0.045$ ) were removed from the original data set as suggested by Vidal et al. (2001). Finally, 271 published analyses of chlorite were selected for further use. The formation temperature of each chlorite was calculated assuming that  $\Sigma\text{Fe}_{\text{chl}} = \text{Fe}^{2+}$  (see the discussion in “Results” section) from the position of the following equilibrium reaction involving chlorite, quartz and  $\text{H}_2\text{O}$  at the given pressure ( $P_{\text{ref}}$ )



The non-ideal part of the activity was described using a regular (symmetric) interaction parameter  $W$  that can be expressed as follows

$$W = a + bT + cP \quad (32)$$

The coefficients  $b$  and  $c$  were first fixed to zero, and only the coefficients  $a$  for all three interaction parameters were refined with the *MEAMP* program by minimizing the sum of the square of  $\Delta G_{\text{reaction}}$  calculated for each analysis at the  $P_{\text{ref}}$  and  $T_{\text{ref}}$  adopted from the original publications. Introducing pressure and temperature dependence of  $W$  (coefficients  $b$  and  $c$  in Eq. 32) did not detectably improve the fit to the natural data, and consequently, all interaction parameters were accepted as constant. The regressed symmetric interaction parameters between sudoite and other chlorite end-

**Table 4** Non-ideal interaction parameters used in the model Chl(LWV) describing the non-ideal interactions on the site M1

	$W_{\text{H}}$ (J/mol)
$W_{\text{am-clin}}$	18,000 <sup>1</sup>
$W_{\text{am-daph}}$	13,500 <sup>1</sup>
$W_{\text{am-sud}}$	43,300 <sup>2</sup>
$W_{\text{clin-daph}}$	2,500 <sup>1</sup>
$W_{\text{clin-sud}}$	49,100 <sup>2</sup>
$W_{\text{daph-sud}}$	43,400 <sup>2</sup>

<sup>1</sup> From Holland et al. (1998) and subsequent updates

<sup>2</sup> Adjusted in this study

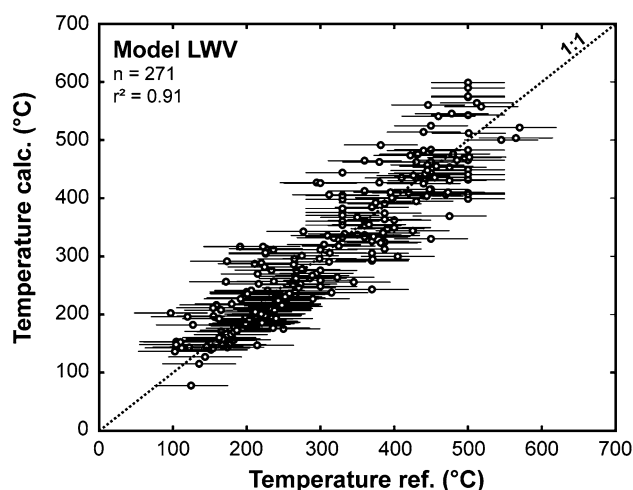


**Fig. 5** Comparison between calculated and reference temperatures (temperature estimates from the original publications) of the natural samples that were used for regressing chlorite model parameters. Due to the absence of appropriate calculations of error propagation in the majority of the original publication, the error bars for the reference temperatures were set to an average value of  $\pm 50$  °C. A total number of 271 natural analyses were finally used

members were found to be high and positive (see details in Table 4), with  $W_{\text{ames-sud}} = 43.3$  kJ,  $W_{\text{clin-sud}} = 49.1$  kJ and  $W_{\text{daph-sud}} = 43.4$  kJ. Such high values are fully compatible with the observed large miscibility gap between the natural di/tri and tri/tri-chlorite, which are found to coexist in low-temperature and low-pressure (LT–LP) aluminous metapelites (see e.g., Theye et al. 1992). The predicted difference between  $\square$ -Mg and  $\square$ -Fe mixing suggests a slightly non-ideal Fe–Mg exchange, in good agreement with the interaction parameter proposed for Fe–Mg mixing on M1 by Holland et al. (1998).

## Results

The new standard state properties of Mg–sudoite and the regular interaction parameters derived as explained above are summarized in Tables 2 and 4. Figure 5 demonstrates that the temperatures ( $T_{\text{calc}}$ ) estimated with Eq. (31) are in

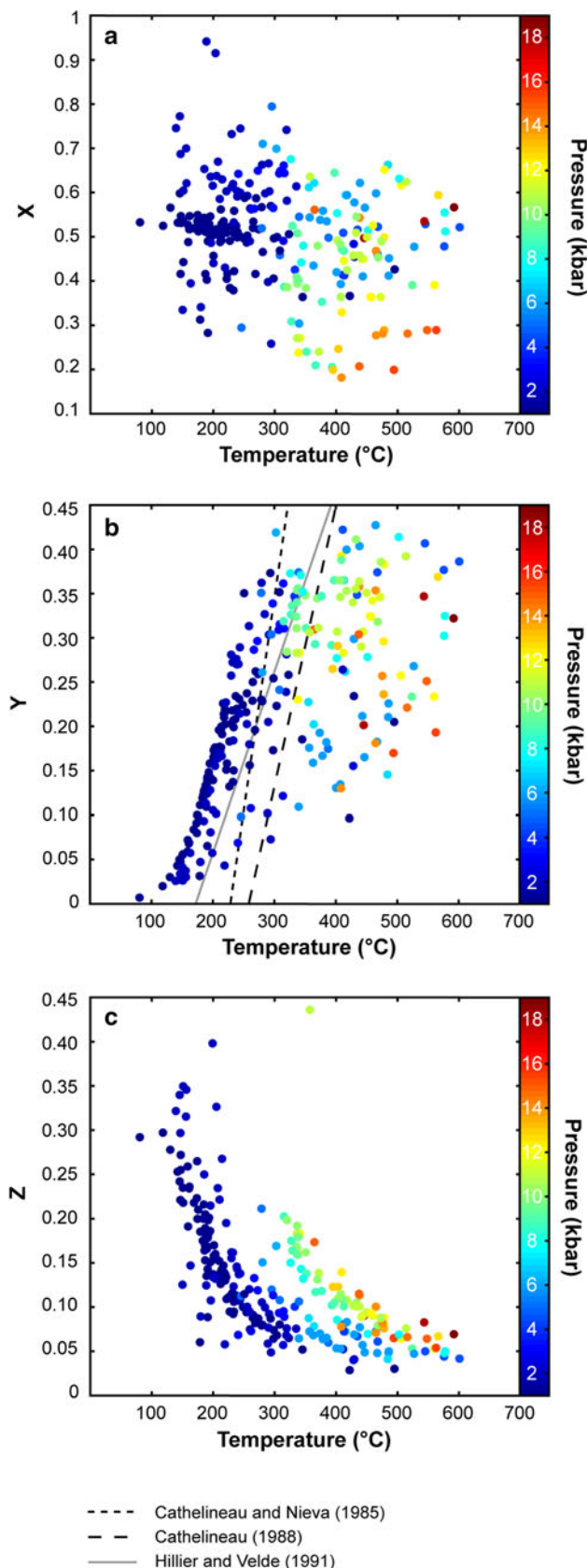


**Fig. 6** Relationships between the different composition variables **a**  $x$ , **b**  $y$  and **c**  $z$  of chlorite minerals and the temperature calculated with the extended chlorite model Chl(LWV). The *color code* of the data points denotes the equilibrium pressure, adopted from the original publications. Because the composition variable  $y$  is linearly correlated with  $X_{\text{Al}}^{\text{M1}}$ , the curves for three empirical chlorite geothermometer calibrations (Cathelineau and Nieva 1985; Cathelineau 1988; Hillier and Velde 1991) are plotted as well. The data show that the number of vacancies ( $z$ ) shows a well defined relationship with temperature

good agreement with the original temperature ( $T_{\text{ref}}$ ;  $R^2 = 0.91$ ). The magnitude of data scatter observed in Fig. 5 is compatible with the uncertainties associated with the  $T_{\text{ref}}$  and  $P_{\text{ref}}$  data reported in the literature sources. It is emphasized that the data in Fig. 5 were calculated assuming that all iron in chlorite is in the ferrous state (because  $\text{Fe}^{3+}$  was not analyzed for most chlorites that were used as input). This assumption has been shown to be incorrect for many natural chlorites (Vidal et al. 2006; Muñoz et al. 2006; Inoue et al. 2009). Therefore, the good fit in Fig. 5 suggests a systematic and continuous evolution of  $(\text{Fe}^{3+}/\Sigma\text{Fe})_{\text{chl}}$  with temperature, as reported by Vidal et al. (2006) who showed that  $(\text{Fe}^{3+}/\Sigma\text{Fe})_{\text{chl}}$  increases with decreasing temperature. The effect of a possible incorporation of  $\text{Fe}^{3+}$  is thus intrinsically included in the derivation of the standard state properties of sudoite and the Margules parameters listed in Tables 2 and 4.

The temperature and pressure dependence of chlorite composition are illustrated in Fig. 6 using the relationship between the composition variables ( $x$ ,  $y$ ,  $z$ ),  $T_{\text{calc}}$  and the original  $P_{\text{ref}}$  data. The first composition variable  $x$  (Eq. 6) does not systematically vary with  $T_{\text{calc}}$  and pressure (Fig. 6a), suggesting that  $x_{\text{Fe}}^{\text{M1}}$  is mainly controlled by the bulk rock composition. The second composition variable  $y$  ( $x_{\text{Al}}^{\text{M1}}$ ) (Eq. 7) increases with temperature (Fig. 6b), although the data show a rather large scatter at temperatures above 300 °C. Only the ames and fames chlorite end-members have Al in the M1 position. These end-members have also Al on T2 and the relationship between  $\text{Al}_{\text{IV}}$  and  $y$  reads:

$$\text{Al}_{\text{IV}} = 1 + y \quad (33)$$

It follows that  $\text{Al}_{\text{IV}}$  should increase with temperature, in agreement with the empirical chlorite thermometers based on the amount of  $\text{Al}_{\text{IV}}$  in chlorite. However, the relation between temperature and  $y$  (or  $\text{Al}_{\text{IV}}$ ) cannot be modeled over the entire temperature range by a simple equation based on the  $\text{Al}_{\text{IV}}$  content only. The temperatures derived with the empirical equations of Cathelineau and Nieva (1985), Cathelineau (1988) and Hillier and Velde (1991) are broadly compatible with the natural data at  $T_{\text{ref}} < 350$  °C, but not with the metamorphic chlorites that formed at higher temperatures (see Fig. 6b). For instance, a chlorite with  $y = 0.15$  is calculated to have formed at 220, 230 and 310 °C using the empirical equations of Hillier and Velde (1991), Cathelineau and Nieva (1985) and



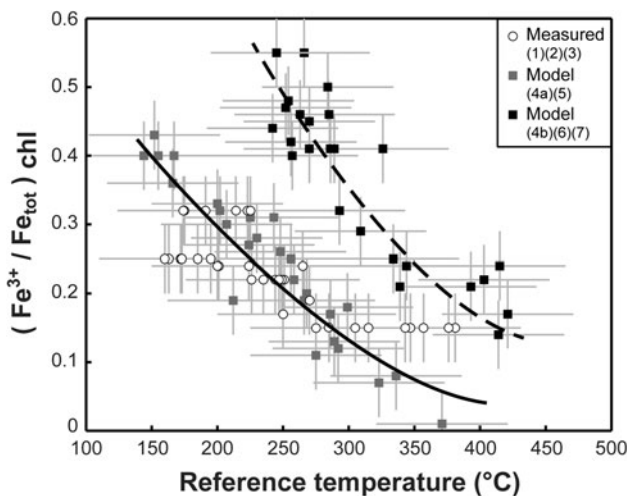


**Fig. 7** Relationships between the  $(\text{Fe}^{3+}/\Sigma\text{Fe})_{\text{chl}}$  value in chlorite and the  $T_{\text{ref}}$  temperature estimates from the original publication. Two main trends are identified depending on the redox conditions, which are less oxidized (*continuous line*) and more oxidized (*dashed line*). (1) Vidal et al. (2006); (2) Inoue et al. (2009); (3) Tarantola et al. (2009); (4) Cantarero et al. (2013) a- Vales Fault; b- Hospital Fault; (5) Lanari et al. (2012); (6) Grosch et al. (2012); (7) Lanari et al. (2013b)

Cathelineau (1988), respectively. By contrast, the natural data show equilibrium temperatures between 180 and 500 °C.

Compared to  $x$  and  $y$ , the third compositional variable  $z$  ( $X_{\square}^{M1}$ ) (Eq. 8) shows a much better correlation with temperature and pressure (Fig. 6c). For a given pressure, the amount of vacancies increases with decreasing temperature and increasing pressure, as already shown by Vidal et al. (2001). These systematic trends suggest that the amount of vacancies is mainly controlled by  $P$  and  $T$  and not by the bulk rock composition (with the assumption that  $\Sigma\text{Fe} = \text{Fe}^{2+}$ ). An empirical calibration based on the amount of vacancies could therefore reproduce the observed trends and thus be used as an empirical thermometer (at given  $P$ ) or, alternatively, as barometer (at given  $T$ ).

### Semi-empirical geothermometers

The Chl(LWV) model described above has been developed for use in phase equilibria computation such as  $P$ – $T$  section modeling. The crystallization temperature of chlorite can be estimated from the equilibrium between chlorite, quartz and water (Eq. 31), but it requires calculation of  $G(P, T)$  as well as the ideal and non-ideal parts of the activity coefficients ( $a_i$  and  $\gamma_i$ ). Because many applications based on field data are only concerned with the chlorite formation temperature, we propose in the following section a simplified procedure (semi-empirical geothermometers) based on the temperature dependence of Eq. (31). Assuming that

the activity of water is unity, the logarithm of the equilibrium constant for Eq. (31) can be expressed as:

$$\ln(K) = \ln\left(\frac{a_{\text{ames}}^4}{a_{\text{clin}}^2 a_{\text{sud}}^3}\right) \quad (34)$$

where  $a_{\text{ames}}$ ,  $a_{\text{clin}}$  and  $a_{\text{sud}}$  are the ideal activities, which are defined in Eqs. (22), (23) and (24), respectively. For reasons of simplicity, only the ideal part of the activity was used to derive the semi-empirical thermometer that links the formation temperature of chlorite with its composition. This simplification results in only small differences between the semi-empirical model and the temperature predicted from the non-ideal Chl(LWV) model (see Inoue et al. 2009; Fig. 9b).

At thermodynamic equilibrium ( $\Delta G_{\text{reaction}} = 0$ ) between chlorite, quartz and water, the logarithm of the equilibrium constant can be expressed as (neglecting  $\Delta C_p$  that is likely not to change much with pressure and temperature):

$$-\ln(K) = \frac{\Delta H^0 + (P - 1)\Delta V^0}{RT} + \frac{\Delta S^0}{R} \quad (35)$$

Different assumptions can be made to compute  $\ln(K)$  regarding the oxidation state of iron in chlorite, which are discussed below.

#### Geothermometer Chl(1): ( $\Sigma\text{Fe} = \text{Fe}^{2+} + \text{Fe}^{3+}$ )

The derivation of the Chl(LWV) model was based on the assumption that all iron in chlorite is in the ferrous state. However, ferric iron is often observed in chlorite (Albee 1962; Vidal et al. 2005, 2006; Muñoz et al. 2006; Tarantola et al. 2009; Inoue et al. 2009, 2010 and references therein). The measurement of  $(\text{Fe}^{3+}/\Sigma\text{Fe})$  in chlorite has been done using different analytical techniques such as Mössbauer spectroscopy (e.g., Inoue et al. 2009 and references therein), X-ray absorption near edge structure (XANES) spectroscopy at the K edge (e.g., Muñoz et al. 2006, 2013; De Andrade et al. 2011) and scanning transmission X-ray microscopy (SXTM; e.g., Bourdelle et al. 2013 and references therein). Vidal et al. (2005, 2006) proposed to estimate the minimum amount of  $\text{Fe}^{3+}$  in chlorite using criteria based on the convergence between the four equilibria written for the assemblage chlorite–quartz–water with the end-members clin, fames, ames and sud (see also Lanari et al. 2012; Grosch et al. 2012; Cantarero et al. 2013). For the studied examples, the  $(\text{Fe}^{3+}/\Sigma\text{Fe})_{\text{chl}}$  values were found to be in good qualitative agreement with  $(\text{Fe}^{3+}/\Sigma\text{Fe})_{\text{chl}}$  values measured by XANES (Muñoz et al. 2006; Vidal et al. 2006).

Measured and estimated  $(\text{Fe}^{3+}/\Sigma\text{Fe})_{\text{chl}}$  values reported in the literature are compared in Fig. 7 against the corresponding temperature conditions which was either calculated with the approach of Vidal et al. (2005, 2006) or

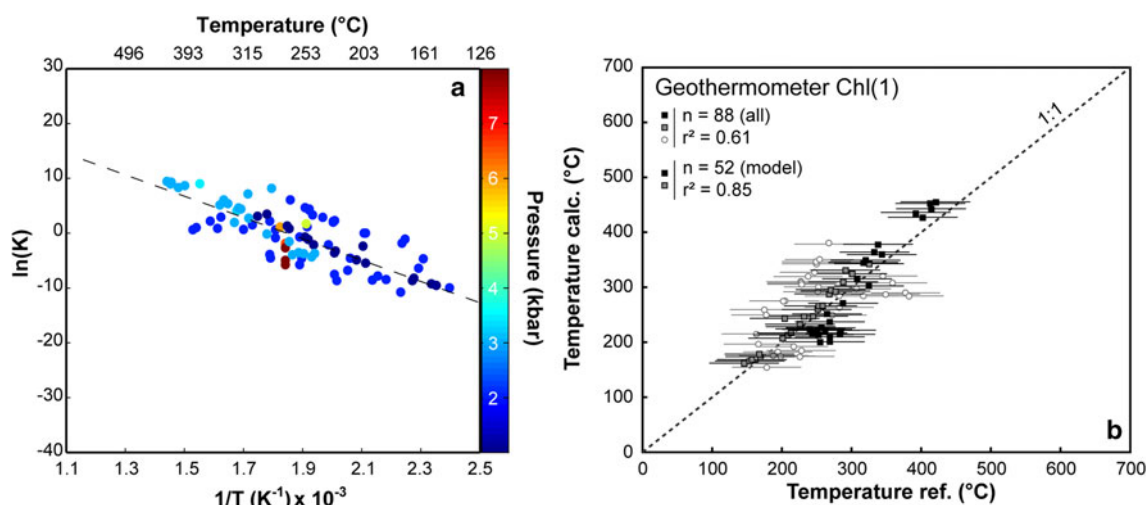
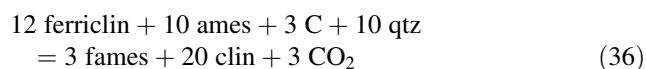


**Fig. 8** Performance of the new semi-empirical chlorite geothermometer Chl(1). **a** Correlation diagram illustrating the relationship between  $1/T$  and the  $\ln(K)$  of Eq. (36). The color code of the data denotes the equilibrium pressure, and the dashed line is the regression

estimated independently. Figure 7 shows that the  $(\text{Fe}^{3+}/\Sigma\text{Fe})$  of chlorite occurring in various geological environments increases with decreasing temperature. In detail, two trends are identified in the Fig. 7, which correspond to chlorite formed at different redox conditions. Chlorite compositions along the trend with the lowest  $\text{Fe}^{3+}$  (solid line and gray squares in Fig. 7) formed under reduced conditions in graphite-bearing metapelites (Vidal et al. 2006) and metasediments (Tarantola et al. 2009; Lanari et al. 2012), and in graphite-absent granodiorites (Vales Fault, Catalan Coastal Ranges, Cantarero et al. 2013). By contrast, chlorite compositions that plot along the trend with the highest  $\text{Fe}^{3+}$  values (dashed line and black squares in Fig. 7) occur in graphite-absent orthogneisses (Lanari et al. 2013b), low-grade metabasalts, altered ultramafic rocks (Grosch et al. 2012) and granodiorites (Hospital Fault, Catalan Coastal Ranges, Cantarero et al. 2013).

Chlorite crystallized in graphite-bearing rocks is thus less oxidized than that crystallized at the same  $P$ – $T$  conditions in graphite-absent rocks. This observation can be explained by the following idealized reaction involving the reduction of ferri-clinocllore (ferriclin:  $\text{Fe}_1^{3+}\text{Mg}_4\text{Al}_1(\text{Si},\text{Al})_2\text{Si}_2\text{O}_{10}(\text{OH})_8$ ) in clinocllore and the oxidation of graphite:



Chlorite crystallizing in graphite-bearing rocks is therefore expected to include less  $\text{Fe}^{3+}$  than chlorite in graphite-absent rocks as observed in Fig. 7. The  $(\text{Fe}^{3+}/\Sigma\text{Fe})_{\text{chl}}$  predicted with the thermodynamic approach proposed by Vidal et al. (2006) is consistent with these trends and the

curve. **b** Comparison between calculated and reference temperatures for natural chlorite samples (see Fig. 7). The error bars for  $T_{\text{chl}}$  were set to an average value of  $\pm 50$  °C

control of the iron oxidation state by redox buffers present in the rock.

An example of this control is provided by the granodiorite from the Catalan Coastal Ranges (Cantarero et al. 2013), which is affected by two different fault systems containing chlorite with two different  $(\text{Fe}^{3+}/\Sigma\text{Fe})_{\text{chl}}$  ratios. Chlorite from the Vales Fault belongs to the less oxidized group, while chlorite from the Hospital Fault belongs to the more oxidized group. No graphite was reported for the less oxidized sample, but the exclusive occurrence of  $\text{Fe}^{3+}$ -rich epidote in the Hospital Fault is consistent with the higher predicted  $(\text{Fe}^{3+}/\Sigma\text{Fe})_{\text{chl}}$  contents.

A first geothermometer termed Chl(1) has been constrained from the set of natural data that were used to compute Fig. 7. The composition variables  $x$ ,  $y$  and  $z$  were calculated using either the measured or estimated  $(\text{Fe}^{3+}/\Sigma\text{Fe})_{\text{chl}}$  value reported in the original publications and assuming that  $\text{Fe}^{3+}$  is restricted to the M4 site (detailed procedure in “Appendix”). Then, the ideal activities  $a_{\text{ames}}$ ,  $a_{\text{clin}}$  and  $a_{\text{sud}}$  were calculated using Eqs. (22), (23) and (24), respectively, and  $\ln(K)$  was obtained from Eq. (34). As expected from Eq. (35),  $\ln(K)$  decreases with  $1/T$  (Fig. 8) and is not dependent on pressure ( $\Delta V^0 \approx 0$ ). The variation in the enthalpy  $\Delta H^\circ$  and entropy  $\Delta S^\circ$  of reaction has been estimated simultaneously by minimizing the temperature difference between  $T_{\text{chl}}$  estimated with Eq. (35) and  $T_{\text{ref}}$ . The regression yields the temperature dependence of  $\ln(K)$  as:

$$-\ln(K) = \frac{172341}{RT} - \frac{315.149}{R} \quad (37)$$

The formation temperature of chlorite can then be calculated for a known  $\ln(K)$  value using the relationship:

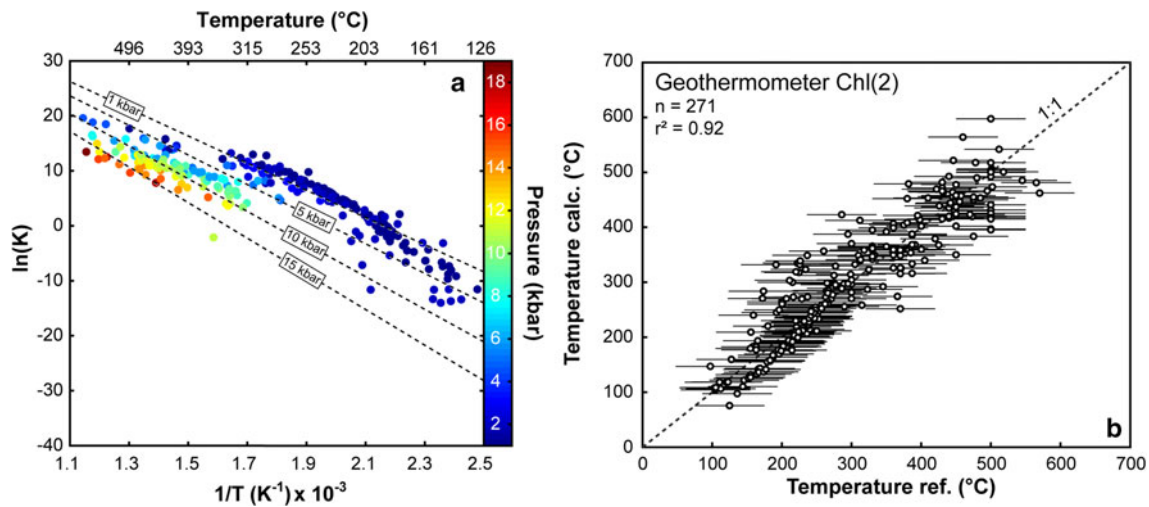


**Fig. 9** Performance of the new semi-empirical chlorite geothermometer Chl(2). **a** Correlation diagram illustrating the relationship between  $1/T$  and the  $\ln(K)$  of Eq. (36). The color code of the data denotes the equilibrium pressure, and dashed lines are the regression curves at different pressures. **b** Comparison between calculated and

reference temperatures for natural chlorite samples. The error bars for  $T_{\text{chl2}}$  were set to an average value of  $\pm 50$  °C. A total number of 271 natural analyses were finally used, and the correlation coefficient is 0.92

$$T_{\text{Chlorite}}(^{\circ}\text{C}) = \frac{172341}{-R \ln(K) + 315.149} - 273.15 \quad (38)$$

The temperatures calculated with Eq. (38) are plotted against the reference temperatures with uncertainties of 50 °C in Fig. 8b. The correlation between  $T_{\text{chl1}}$  and  $T_{\text{ref}}$  is good for the  $(\text{Fe}^{3+}/\Sigma\text{Fe})_{\text{chl}}$  ratio predicted with the thermodynamic approach proposed by Vidal et al. (2006) ( $R^2 = 0.85$ ,  $n = 52$ ). It is somewhat worse when including the  $(\text{Fe}^{3+}/\Sigma\text{Fe})_{\text{chl}}$  measured with Mössbauer spectrometry ( $R^2 = 0.61$ ), although the measured values follow the same general trend, i.e., the  $\text{Fe}^{3+}$  content increases with decreasing temperature. The lower correlation coefficient reflects significant scatter of the  $(\text{Fe}^{3+}/\Sigma\text{Fe})_{\text{chl}}$  values that were measured by Mössbauer spectrometry, probably because the reported values are average values from bulk samples that likely include chlorites grains of differing  $\text{Fe}^{3+}$  content (Inoue et al. 2009) which possibly formed at different temperature conditions.

The Chl(1) geothermometer requires prior and accurate knowledge of the  $(\text{Fe}^{3+}/\Sigma\text{Fe})_{\text{chl}}$  values of individual chlorite grains, which is a serious limitation for its practical use, especially for polymetamorphic rock that contains several generations of chlorites with differing  $(\text{Fe}^{3+}/\Sigma\text{Fe})_{\text{chl}}$ .

#### Geothermometer Chl(2): ( $\Sigma\text{Fe} = \text{Fe}^{2+}$ )

Addressing the restrictions of the Chl(1) geothermometer, a second geothermometer termed Chl(2) has been derived based on the assumption that all iron in chlorite is in the ferrous state ( $\Sigma\text{Fe} = \text{Fe}^{2+}$ ).

Figure 9a shows a plot of  $\ln(K)$  against  $1/T$  using the same set of natural chlorite compositions that were used to constrain the thermodynamic model Chl(LWV) and the reference formation temperatures ( $T_{\text{ref}}$ ). This diagram demonstrates that  $\ln(K)$  decreases with  $1/T$  as predicted by Eq. (35), and further illustrates that when assuming ( $\Sigma\text{Fe} = \text{Fe}^{2+}$ ),  $\ln(K)$  is also dependent on pressure. The reaction properties  $\Delta H^{\circ}$ ,  $\Delta V^{\circ}$  and  $\Delta S^{\circ}$  have been estimated simultaneously by minimizing the temperature difference between  $T_{\text{chl2}}$  estimated with Eq. (35) and  $T_{\text{calc}}$  estimated using the Chl(LWV) model. The regression leads to the following pressure and temperature dependence of  $\ln(K)$ :

$$-\ln(K) = \frac{203093 + 4996.99P}{RT} - \frac{455.782}{R} \quad (39)$$

This relationship is plotted onto the correlation diagram of  $\ln(K)$  versus  $1/T$  (Fig. 7a) for pressures of 1, 5, 10 and 15 kbar. The temperature of chlorite can then be calculated for a known  $\ln(K)$  value using the relationship:

$$T_{\text{Chlorite}}(^{\circ}\text{C}) = \frac{203093 + 4996.99P(\text{kbar})}{-R \ln(K) + 455.782} - 273.15 \quad (40)$$

The temperatures calculated with Eq. (40) are plotted against the reference temperatures with uncertainties of 50 °C in Fig. 7b. The correlation between the original temperature estimates and  $T_{\text{chl2}}$  using Eq. (40) shows that ignoring the non-ideal part of the activities in Eq. (35) does not introduce a detectable scatter in the distribution of the data. The semi-empirical calibration predicts correct temperatures over the range 100–500 °C and for the pressure

range 1–20 kbar. With the assumption  $\Sigma\text{Fe} = \text{Fe}^{2+}$ , the chlorite temperature can be estimated using either the full thermodynamic approach in conjunction with the estimation of the position of the chlorite–quartz–water equilibrium curve (Chl(LWV) model) or the semi-empirical relationship (Eq. 40) for the same equilibrium.

#### Ideal activity models for the semi-empirical chlorite geothermometers

The new semi-empirical geothermometers Chl(1) and Chl(2) use an ideal activity model as initially proposed by Walshe (1986) and Inoue et al. (2009). Thorough comparison between  $T_{\text{chl1}}$ ,  $T_{\text{chl2}}$  and the original  $T_{\text{ref}}$  shows that this assumption is reasonably valid for estimating the temperature of chlorite formation. However, this approach cannot be used in the framework of the Holland–Powell internally consistent data set, because non-ideality is required to account for immiscibility between chlorite and sudoite.

## Applications and discussion

#### Phase diagram calculations

The new solid solution model Chl(LWV) is compatible with the thermodynamic database of Holland and Powell (1998), and it can be used for phase diagram calculations such as  $P$ – $T$  section modeling. The model is compatible with the data structure of all major petrological packages, including *THERMOCALC* (Powell et al. 1998; Powell and Holland 2008), *Perple\_X* (Connolly 2005, 2009; Connolly and Petrini 2002) and *Theriak-Domino* (de Capitani and Petrakakis 2010) and has been included into the *Perple\_X* program version 6.6.8. Details concerning the *Perple\_X* coding can be found in the Supplementary Material.

As discussed above, the occurrence and composition of chlorite minerals in diverse geological environments are controlled by both the bulk rock composition and the equilibrium conditions. For certain bulk rock compositions, trioctahedral chlorite and sudoite have been observed to coexist in the same equilibrium mineral assemblage. Sudoite is well known in sedimentary, diagenetic and hydrothermal environments and has also been described from low-grade aluminous metapelites (Goffé 1982; François and Schreyer 1984; Goffé et al. 1988; Franceschelli et al. 1989; Percival and Kodama 1989; Anceau 1992; Theye et al. 1992; Vidal et al. 1992; Billault et al. 2002). In retrogressed high-pressure low-temperature metapelites, assemblages involving sudoite + chlorite + phengite + quartz are found to form after the destabilization of the carpholite + chlorite + phengite  $\pm$  chloritoid

assemblage. Three bulk rock compositions from the study of Theye et al. (1992) have therefore been used to compare  $P$ – $T$  sections calculated with the Chl(HP) and Chl(LWV) solid solution models.

In eastern Crete, sudoite is found in the phyllite-quartzite unit, which is mainly composed of low-grade metasediments (Theye et al. 1992). In this unit, the peak metamorphic temperature–pressure conditions reached during the Alpine orogeny have been estimated at  $300 \pm 50$  °C and  $9 \pm 3$  kbar (Theye and Seidel 1991). The sample *K84/204* described by Theye et al. (1992) represents a greenschist with the main mineral assemblage composed of quartz (>20 vol%), sudoite (<20 vol%), chlorite (<20 vol%) and phengite (<20 vol%). Two  $P$ – $T$  sections were calculated in the CaK FeO–MgO–Al<sub>2</sub>O<sub>3</sub>–SiO<sub>2</sub>–H<sub>2</sub>O (FMASH) system using the solid solution models of Coggon and Holland (2002) for phengite, and Holland and Powell (1998) for plagioclase, staurolite and garnet. Ideal mixing of Fe and Mg was assumed for carpholite and chloritoid. The first  $P$ – $T$  section (Fig. 10b) has been calculated using the Chl(HP) solid solution model (Holland et al. 1998) and the Holland and Powell (1998) data for the standard state thermodynamic properties of sudoite. In this  $P$ – $T$  section, only one chlorite phase without structural vacancies is stable. At 300 °C and 9 kbar, the predicted stable assemblage is composed of chlorite (5 vol%), chloritoid (5 vol%), carpholite (9 vol%), phengite (11 vol%), and quartz (70 wt%). Two main problems are identified in this  $P$ – $T$  section. First, sudoite is not predicted to be stable at these conditions, which contrasts with the observed mineral assemblage. Second, both carpholite and chloritoid are predicted to be stable at 3.8 kbar and 300 °C, which are unrealistically low limiting pressure–temperature conditions for these phases. The second  $P$ – $T$  section (Fig. 10a) has been calculated using the new extended Chl(LWV) chlorite solid solution model and the new thermodynamic standard state properties for sudoite derived in this study. In contrast to the previously calculated  $P$ – $T$  section, (1) two chlorite phases with different compositions coexist at 300 °C and 9 kbar; (2) sudoite-rich chlorite (16 vol%) and tri/trioctahedral chlorite (6 vol%), coexist with phengite (11 vol%), and quartz (67 vol%); and (3) the lower pressure stability limit of the carpholite–chloritoid assemblage is much higher and lies at 11 kbar at 380–400 °C. The mineralogical evolution and the  $P$ – $T$  slope of this reaction are consistent with experimental results (Vidal et al. 1992) and natural observations (Theye and Seidel 1991).

In the same phyllite-quartzite unit described above, sample *K84/02* from Theye et al. (1992) represents a greenschist with the main mineral assemblage composed of quartz (>20 vol%), chlorite (>20 vol%), pyrophyllite (>20 vol%) and phengite (>20 vol%). At 350 °C and



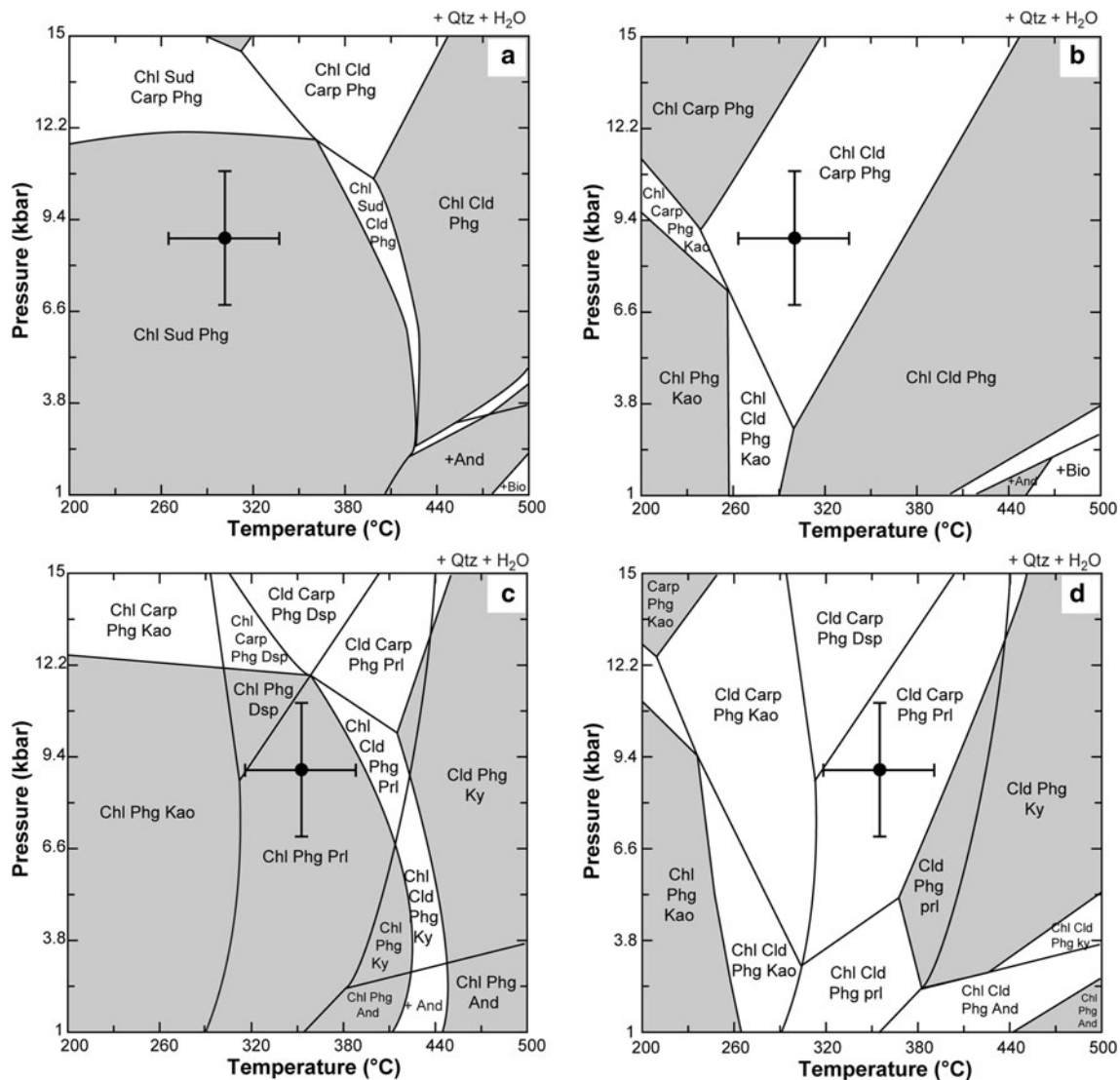


**Fig. 10** *P*–*T* sections calculated in the KFMASH system for the samples *K84/204* (**a**, **b**) and *K84/02* (**c**, **d**) of Theye et al. (1992). The *P*–*T* sections were calculated with *Perple\_X* using chlorite solution models from (**b**, **d**) Holland et al. (1998) and (**a**, **c**) this study. Mineral abbreviations: andalusite (And), carpholite (Carp), chlorite (Chl),

chloritoid (Cld), diaspore (Dsp), garnet (Gt), glaucophane (Gl), jadeite (Jd), kaolinite (Kao), Mg-stilpnomelane (Mstl), paragonite (Pg), phengite (Phg), quartz (Qtz), sillimanite (Sill), stilpnomelane (Stlp), sudoite (Sud)

9 kbar, the stable assemblage calculated using the Chl(HP) solid solution model (Holland et al. 1998) and the thermodynamic standard state properties for sudoite from Holland and Powell (1998) is composed of chloritoid (14 vol%), carpholite (7 vol%), phengite (22 vol%), pyrophyllite (1 vol%) and quartz (51 vol%; Fig. 10d). As observed above for sample *K84/204*, the stability of chloritoid and carpholite contrasts with the observed mineral assemblage. The stable assemblage calculated at 350 °C and 9 kbar with the Chl(LWV) chlorite solid solution model is composed of chlorite (27 vol%), phengite (21 vol%), pyrophyllite (1 vol%) and quartz (51 vol%; Fig. 10c). The predicted mineral assemblage is in excellent

agreement with the natural assemblage observed by Theye et al. (1992).

### Geothermometry

The new semi-empirical geothermometer Chl(2) can be used for a wide range of chlorite compositions, which occur in diverse geological environments such as sedimentary, hydrothermal and low-grade metamorphic systems. The semi-empirical calibration Chl(2) derived above has been implemented into the *XMapTools* package (Lanari et al. 2014; <http://www.xmaptools.com>), a program for processing of X-ray electron microprobe images, mineral



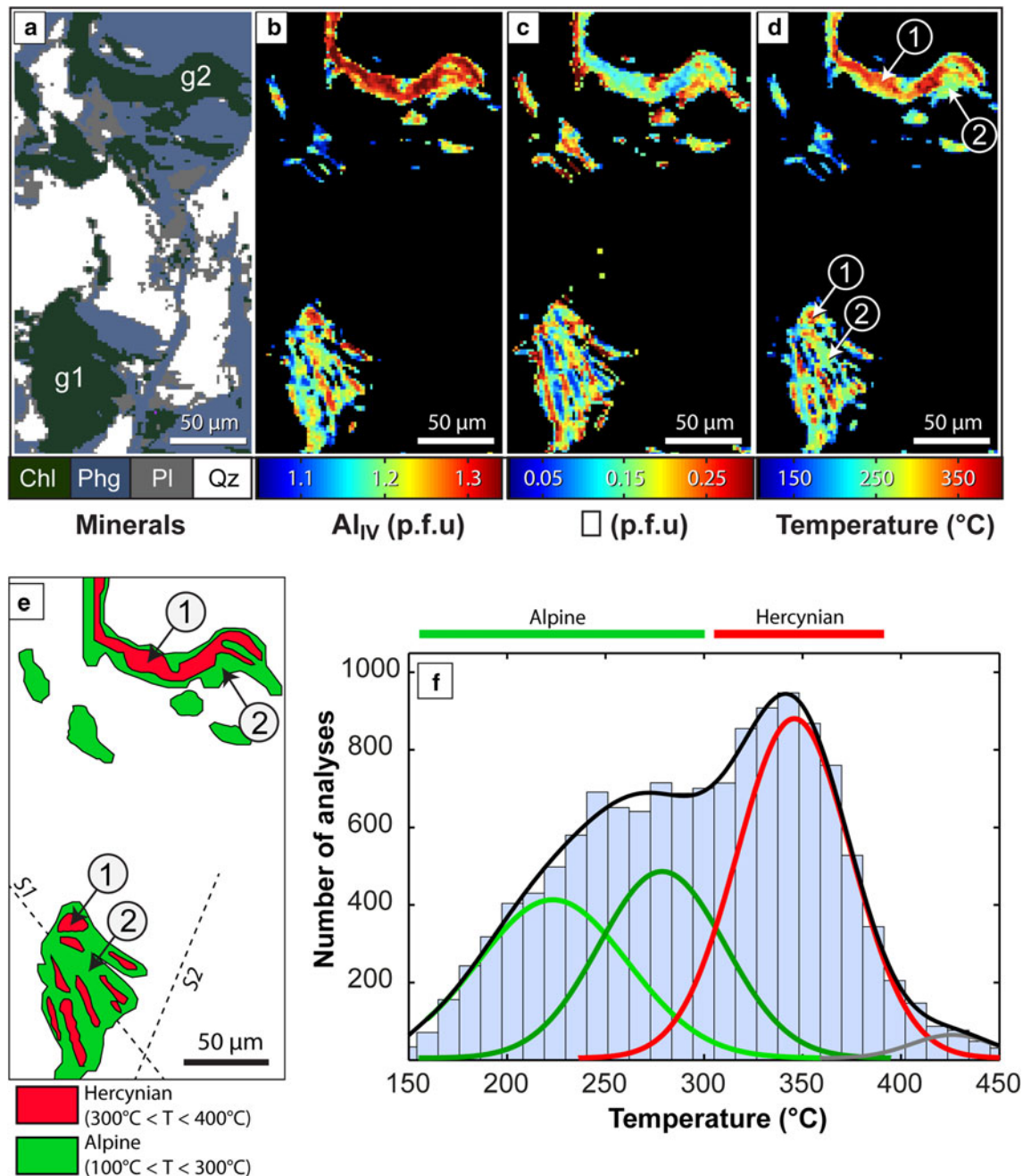


**Fig. 11** Chlorite thermometry applied to electron microprobe X-ray maps from Lanari et al. (2012). **a** Mask image that allocates each pixel to a mineral. **b** Compositional map for Al<sub>IV</sub> (per formula unit, p.f.u.) of chlorite pixels. **c** Compositional map of vacancies (□) of chlorite pixels. **d** Chlorite formation temperatures calculated from Eq. (36) for a pressure of 5 kbar. In **d** and **e**, grains labeled with (1) are Hercynian detrital minerals (see details in Lanari et al. 2012) with

formation temperatures of 300–400 °C, whereas grains labeled with (2) are chlorites that have recrystallized during Alpine metamorphism. These show systematically lower temperatures in the range of 200–275 °C. **f** Histogram of the formation temperatures calculated for the chlorite composition of the entire X-ray maps from Lanari et al. (2012)

classification (Martin et al. 2013) and geothermobarometric calculations (Lanari et al. 2013a). *XMapTools* has been used to calculate the temperature distribution of partially recrystallized detrital chlorite, which have variable (Fe<sup>3+</sup>/ΣFe)<sub>chl</sub> contents (Lanari et al. 2012).

In low-grade metamorphic terrains, one of the main challenges for deriving the *P–T* paths recorded by the rocks and their mineral assemblages is the distinction between detrital and neo-formed minerals, especially when the detrital minerals are partially recrystallized. For instance, in

the western Alps, the external part of the Briançonnais Zone known as the Zone houillère is made up of a stack of Carboniferous and Permian metasediments and metavolcanics. The metasediments are composed of organic-matter-rich schists with intercalations of sandstones with a poorly defined mineralogy including detrital and neo-formed chlorite and K-white mica grains (Gabalda et al. 2009; Lanari et al. 2012). The compositional variations in phyllosilicates were studied in detail by Lanari et al. (2012) using X-ray mapping techniques [see de Andrade et al. (2006) and Lanari et al. (2014) for details about instrumental settings and standardization]. Two distinct metamorphic events were identified, one Hercynian event that is recorded in the detrital minerals and a second Alpine event recorded in neo-formed minerals. We used a representative selection of the X-ray images from Lanari et al. (2012) and applied the following sequence of data processing operations in *XMapTools* (Lanari et al. 2014): (1) Pixels were allocated to a mineral phase using a statistical approach (mask image in Fig. 11a), (2) the raw X-ray maps were transformed into maps of oxide composition using selected fully quantitative point analyses as internal standards, (3) maps of oxide composition were transformed into maps of structural formulae (Fig. 11b, c) and (4) crystallization temperatures of chlorite pixels (Fig. 11d) were estimated using the semi-empirical thermometer Chl(2) (Eq. 39 and “Appendix”).

In the studied thin section area, two chlorite grains are distinguished. The first grain labeled *g1* in Fig. 11a is a detrital grain with a size of 50 by 75  $\mu\text{m}^2$  and shows strong microfracturing with recrystallization of layers parallel to the S1 schistosity. The second grain labeled *g2* is a detrital grain with a size of 150 by 25  $\mu\text{m}^2$  that was kinked during the Alpine deformation event (S2 schistosity).

Maps of  $\text{Al}_{\text{IV}}$  and  $\square$  are displayed in Fig. 11b, c, respectively, and they reveal a strong zoning in the  $\text{Al}_{\text{IV}}$  and  $\square$  contents of both chlorite grains. The grain *g2* shows a core rich in  $\text{Al}_{\text{IV}}$  and poor in  $\square$  and a rim with lower  $\text{Al}_{\text{IV}}$  and higher  $\square$  contents (Fig. 11b, c). This decrease in  $\text{Al}_{\text{IV}}$  and increase in  $\square$  from core to rim is compatible with a decrease in formation temperature. The grain *g1* is more complicated with both  $\text{Al}_{\text{IV}}$  rich and  $\square$  rich layers parallel to S1 (Fig. 11b, c). The chlorite formation temperature has been calculated for each chlorite pixel, and the result is displayed in Fig. 11d. Two distinct groups of chlorite temperatures can be identified in this map. The group 1 in Fig. 11d, e that corresponds to the core of grain *g2* and bands in the *g1* grains shows temperatures between 350 and 400 °C. In contrast, the rims of both grains (group 2 in Fig. 11d, e) show lower calculated formation temperatures between 200 and 275 °C. These data are straightforwardly interpreted such that the detrital part of the grains formed at high temperature between 300 and 400 °C and was overgrown during the Alpine event

by a second generation of chlorite crystallizing at considerably lower temperature.

Subsequently, we have calculated the formation temperature of chlorite of the entire X-ray maps published by Lanari et al. (2012). The temperature histogram has been decomposed into four components using a nonlinear optimization algorithm assuming a Gaussian distribution (Fig. 11f). Three groups of chlorite are distinguished with formation temperatures of  $350 \pm 50$ ,  $275 \pm 50$  and  $210 \pm 50$  °C, respectively. The first group corresponds to the detrital Hercynian chlorite and the two other groups to Alpine events. These results are in very good agreement with the *P–T* paths proposed in Lanari et al. (2012) based on independent approaches.

## Conclusions

An extended activity-composition model for di-trioctahedral chlorite in the FMASH system has been calibrated, which has been derived based on the Holland–Powell internally consistent thermodynamic data set. The new model is formulated in terms of four linearly independent end-members, which are amesite, clinocllore, daphnite and sudoite, and accounts for Fe–Mg, Tschermarks and vacancy substitution. The ideal part of the activity of the chlorite end-members is described with a mixing-on-site model and the non-ideal part with a macroscopic symmetric formalism. The symmetric interaction parameters between sudoite and the other independent end-members have been simultaneously refined using a set of 271 published analyses of chlorite (with the assumption that  $\Sigma\text{Fe} = \text{Fe}^{2+}$ ) for which independent temperature estimates are available. The model was also calibrated using experimental data for the reaction carpholite = sudoite + quartz + water, which made it possible to refine the standard state properties of sudoite. Update of the sudoite thermodynamic properties was required to reproduce the solvus between tri/trioctahedral chlorite and di/trioctahedral sudoite occurring in low-grade metapelites. *P–T* sections calculated with the new model predict mineral assemblages and modes for aluminous metapelites that are in good agreement with observed natural assemblages. The new model Chl(LWV) is compatible with phase equilibria computation programs such as *Perple\_X*, *THERMOCALC* and *Theriak-Domino* and with other software that is used to compute fluid-mineral equilibria (Dolejs and Wagner 2008) such as *GEM-Selektor* (Karpov et al. 1997; Wagner et al. 2012; Kulik et al. 2013). Based on the new thermodynamic model, two semi-empirical calibrations were derived. Chl(1) explicitly accounts for  $\text{Fe}^{3+}$  and requires that accurate measurements of the  $(\text{Fe}^{3+}/\Sigma\text{Fe})_{\text{chl}}$  value of chlorite are available. Chl(2) can

be used for chlorite geothermometry over the  $P$ – $T$  range 100–500 °C and 1–20 kbar when the  $(\text{Fe}^{3+}/\Sigma\text{Fe})_{\text{chl}}$  value is unknown. Both semi-empirical calibrations have been included into the software package *XMapTools* that allows computing of chlorite formation temperature maps from electron -microprobe X-ray maps. The geothermometers are useful for a large variety of chlorite, ranging from sedimentary to hydrothermal and metamorphic environments.

**Acknowledgments** The authors sincerely thank James Connolly, Martin Engi, Eric Lewin, Emilie Janots and Nicolas Riel for fruitful discussions. Constructive reviews from J. Walshe and an anonymous reviewer are gratefully acknowledged. This work was financially supported by the Agence National pour la Recherche (ANR) ERD-Alps project and the Ecole doctorale Terre-Univers-Environnement travel grant.

## Appendix: From structural formulae to composition variables

The calculation is based on a structural formula of chlorite (normalized on the basis of 14 oxygen atoms) where the concentrations of Si, Ti, Al,  $\text{Fe}^{2+}$ ,  $\text{Fe}^{3+}$ , Mg, Na, Ca and K are known in atoms per formula unit (p.f.u.). From the structural formula, the composition variables  $x$ ,  $y$  and  $z$  (Eqs. 6, 7 and 8, respectively) can be derived using the following approach: (1)

$$X^{\text{Fe}} = \text{Fe}^{2+} / (\text{Fe}^{2+} + \text{Mg})$$

$$x = X^{\text{Fe}}$$

(2)

$$\text{Al}_{\text{IV}} = 4 - (\text{Si} + \text{Ti})$$

$$\text{Al}_{\text{VI}} = \text{Al}_{\text{total}} - \text{Al}_{\text{IV}}$$

$$R1 = \text{Na} + \text{K};$$

$$\square = 1/2 (\text{Al}_{\text{VI}} - \text{Al}_{\text{IV}} + \text{Fe}^{3+} - R1)$$

$$z = \square$$

(3)

$$\text{Al}^{\text{M4}} = 1 - \text{Fe}^{3+}$$

$$\text{Al}^{\text{M23}} = 2\square^{\text{M1}}$$

$$\text{Al}^{\text{M1}} = \text{Al}_{\text{VI}} - (\text{Al}^{\text{M23}} + \text{Al}^{\text{M4}})$$

$$y = \text{Al}^{\text{M1}}$$

## References

- Abad I, Nieto F, Peacor D, Velilla N (2003) Prograde and retrograde diagenetic and metamorphic evolution in metapelitic rocks of Sierra Espuna (Spain). *Clay Miner* 38:1–23
- Agard P, Vidal O, Goffé B (2001) Interlayer and Si content of phengite in HP–LT carpholite-bearing metapelites. *J Metam Geol* 19:479–495
- Agard P, Monié P, Gerber W, Omrani J, Molinaro M, Meyer B, Labrousse L, Vrielynck B, Jolivet L, Yamato P (2006) Transient, synobduction exhumation of Zagros blueschists inferred from P–T, deformation, time, and kinematic constraints: implications for Neotethyan wedge dynamics. *J Geophys Res* 111:B11401
- Albee AL (1962) Relationships between the mineral association, chemical composition and physical properties of the chlorite series. *Am Miner* 47:851–870
- Anceau A (1992) Sudoite in some Visean (lower Carboniferous) K-bentonites from Belgium. *Clay Miner* 27:283–292
- Árkai P, Faryad SW, Vidal O, Balogh K (2003) Very low-grade metamorphism of sedimentary rocks of the Meliata unit, Western Carpathians, Slovakia: implications of phyllosilicate characteristics. *Int J Earth Sci* 92:68–85
- Augier R, Booth-Rea G, Agard P, Martínez-Martínez JM, Jolivet L, Azanón JM (2005a) Exhumation constraints for the lower Nevado-Filabride complex (Betic cordillera, SE Spain): a thermometry and TWEEQU multiequilibrium thermobarometry approach. *Bull Soc Geol France* 176:403–416
- Augier C, Agard P, Monié P, Jolivet L, Robin C, Booth-Rea G (2005b) Exhumation, doming and slab retreat in the Betic Cordillera (SE Spain): in situ  $^{40}\text{Ar}/^{39}\text{Ar}$  ages and P–T–d–t paths for the Nevado-Filabride complex. *J Metam Geol* 23:357–381
- Baboury D (1999) Origine volcanogène des veines aurifères riches en sulfures de la mine Géant Dormant, Abitibi. PhD thesis, Université du Québec à Chicoutimi
- Baker J, Holland T (1996) Experimental reversals of chlorite compositions in divariant  $\text{MgO} + \text{Al}_2\text{O}_3 + \text{SiO}_2 + \text{H}_2\text{O}$  assemblages. *Am Miner* 81:676–684
- Belmar M, Morata D (2005) Nature and P–T–t constraints of very low-grade metamorphism in the Triassic–Jurassic basins, coastal range, central Chile. *Rev Geol Chile* 32:189–205
- Berman R (1988) Internally-consistent thermodynamic data for minerals in the system  $\text{Na}_2\text{O} - \text{K}_2\text{O} - \text{CaO} - \text{MgO} - \text{FeO} - \text{Fe}_2\text{O}_3 - \text{Al}_2\text{O}_3 - \text{SiO}_2 - \text{TiO}_2 - \text{H}_2\text{O} - \text{CO}_2$ . *J Petrol* 29:445–522
- Berman R, Brown T (1985) Heat capacity of minerals in the system  $\text{Na}_2\text{O} - \text{K}_2\text{O} - \text{CaO} - \text{MgO} - \text{FeO} - \text{Fe}_2\text{O}_3 - \text{Al}_2\text{O}_3 - \text{SiO}_2 - \text{TiO}_2 - \text{H}_2\text{O} - \text{CO}_2$ : representation, estimation, and high temperature extrapolation. *Contrib Mineral Petrol* 89:168–183
- Billault V, Beaufort D, Patrier-Mas P, Petit S (2002) Crystal chemistry of Fe-sudoites from uranium deposits in the Athabasca basin (Saskatchewan, Canada). *Clays Clay Miner* 50:70–81
- Booth-Rea G, Azanón J, Goffé B, Vidal O, Martínez-Martínez J (2002) High-pressure, low-temperature metamorphism in Alpujarride units of southeastern Betics (Spain). *Compt Rend Geosci* 334:857–865
- Bourdelle F, Parra T, Chopin C, Beyssac O (2013a) A new chlorite geothermometer for diagenetic to low-grade metamorphic conditions. *Contrib Mineral Petrol* 165:723–735
- Bourdelle F, Parra T, Beyssac O, Chopin C, Vidal O (2013b) Clay minerals thermometry: a comparative study based on high-resolution chemical analyses of illite and chlorite in sandstones from the Gulf Coast (Texas, USA). *Am Miner* 98:914–926
- Bourdelle F, Benzerara K, Beyssac O, Cosmidis J, Neuville DR, Brown GE, Paineau E (2013c) Quantification of the ferric/ferrous iron ratio in silicates by scanning transmission X-ray microscopy at the Fe  $L_{2,3}$  edges. *Contrib Mineral Petrol* 166:423–434
- Calderon M, Galaz G, Tascon G, Ramirez C, Luca R, Zenk M, Brandelik A, Hervé F (2005) Metamorphic P–T constraints for non-coaxial ductile flow of Jurassic pyroclastic deposits: key evidence for the closure of the Rocas Verdes Basin in Southern

- Chile. 6th international symposium on andean geodynamics (ISAG 2005, Barcelona)
- Cantarero I, Lanari P, Vidal O, Alias G, Travé A, Baqués V (2013) Long-term fluid circulation in extensional faults in the central catalan coastal ranges: P-T constraints from neofomed chlorite and K-white mica. *Int J Earth Sci*. doi:[10.1007/s00531-013-0963-8](https://doi.org/10.1007/s00531-013-0963-8)
- Cathelineau M (1988) Cation site occupancy in chlorites and illites as function of temperature. *Clay Miner* 23:471–485
- Cathelineau M, Nieva D (1985) A chlorite solid solution geothermometer the Los Azufres (Mexico) geothermal system. *Contrib Mineral Petrol* 91:235–244
- Chopin C (1979) De la Vanoise au Grand Paradis, une approche pétrographique et radiochronologique de la signification géodynamique du métamorphisme de haute pression. PhD thesis, University of Pierre et Marie Curie Paris VI
- Coggon R, Holland T (2002) Mixing properties of phengitic micas and revised garnet-phengite thermobarometers. *J Metam Geol* 20:683–696
- Connolly JAD (2005) Computation of phase equilibria by linear programming: a tool for geodynamic modeling and its application to subduction zone decarbonation. *Earth Planet Sci Lett* 236:524–541
- Connolly JAD (2009) The geodynamic equation of state: what and how. *Geochem Geophys Geosyst* 10:1–19
- Connolly JAD, Petrin K (2002) An automated strategy for calculation of phase diagram sections and retrieval of rock properties as a function of physical conditions. *J Metam Geol* 20:697–708
- de Andrade V, Vidal O, Lewin E, O'Brien P, Agard P (2006) Quantification of electron microprobe compositional maps of rock thin sections: an optimized method and examples. *J Metam Geol* 24:655–668
- de Andrade V, Susini J, Salomé M, Beraldin O, Rigault C, Heymes T, Lewin E, Vidal O (2011) Submicrometer hyperspectral X-ray imaging of heterogeneous rocks and geomaterials: applications at the Fe K-edge. *Anal Chem* 83:4220–4227
- de Capitani C, Petrakakis K (2010) The computation of equilibrium assemblage diagrams with Theriak/Domino software. *Am Miner* 95:1006–1016
- de Caritat P, Hutcheon I, Walshe J (1993) Chlorite geothermometry: a review. *Clays Clay Miner* 41:219–239
- Dolejs D, Wagner T (2008) Thermodynamic modeling of non-ideal mineral-fluid equilibria in the system Si–Al–Fe–Mg–Ca–Na–K–H–O–Cl at elevated temperatures and pressures: implications for hydrothermal mass transfer in granitic rocks. *Geochim Cosmochim Acta* 72:526–553
- Dubacq B, Vidal O, de Andrade V (2009) Dehydration of dioctahedral aluminous phyllosilicates: thermodynamic modelling and implications for thermobarometric estimates. *Contrib Mineral Petrol* 159:159–174
- Franceschelli M, Mellini M, Memmi I (1989) Sudoite, a rock-forming mineral in Verrucano from the Northern Apennines (Italy) and the sudoite–chloritoid–pyrophyllite assemblage in prograde metamorphism. *Contrib Mineral Petrol* 101:274–279
- Fransolet A, Schreyer W (1984) Sudoite, di/trioctahedral chlorite: a stable low-temperature phase in the system MgO–Al<sub>2</sub>O<sub>3</sub>–SiO<sub>2</sub>–H<sub>2</sub>O. *Contrib Mineral Petrol* 86:409–417
- Gabalda S, Beyssac O, Jolivet L, Agard P, Chopin C (2009) Thermal structure of a fossil subduction wedge in the Western Alps. *Terra Nova* 21:28–34
- Ganne J, Bussy F, Vidal O (2003) Multi-stage garnet in the internal Briançonnais basement (Ambin Massif, Savoy): new petrological constraints on the blueschist-facies metamorphism in the Western Alps and tectonic implications. *J Petrol* 44:1281
- Ganne J, de Andrade V, Weinberg RF, Vidal O, Dubacq B, Kagambega N, Naba S, Baratoux L, Jessell M, Allibon J (2012) Modern-style plate subduction preserved in the Palaeoproterozoic West African craton. *Nat Geosci* 5:60–65
- Goffé B (1982) Définition du faciès Fe–Mg carpholite–chloritoid, un marqueur du métamorphisme de HP–BT dans les métasédiments alumineux. PhD thesis, Université de Paris VI
- Goffé B, Bousquet R (1997) Ferrocapholite, chloritoïde et lawsonite dans les métapélites des unités du Versoyen et du Petit St Bernard (zone valaisanne, Alpes occidentales). *Schweizer Mineral Petrogr Mitt* 77:137–147
- Goffé B, Michard A, Kienast JR, Le Mer O (1988) A case of obduction-related high pressure, low temperature metamorphism in upper crustal nappes, Arabian continental margin. Oman: P–T paths and kinematic interpretation. *Tectonophysics* 151:363–386
- Grosch EG, Vidal O, Abu-Alam T, McLoughlin N (2012) PT-constraints on the metamorphic evolution of the Paleoproterozoic Kromberg type-section, Barberton Greenstone Belt, South Africa. *J Petrol* 53:513–545
- Halter WH, Williams-Jones AE, Kontak DJ (1998) Modeling fluid-rock interaction during greisenization at the East Kemptville tin deposit: implications for mineralization. *Chem Geol* 150:1–17
- Hannula K, Lackey J, Mattox E, Mcgrath G, Onasch E, Wertim J (1999) Syn-tectonic pluton intrusion during contractional deformation: microstructural and metamorphic evidence from the aureole of the Acadian Victory Pluton, north-eastern Vermont, USA. *J Metam Geol* 17:271–286
- Hillier S, Velde B (1991) Octahedral occupancy and chemical composition of diagenetic (low-temperature) chlorites. *Clay Miner* 26:149–168
- Hoisch T (2000) Conditions of metamorphism in lower-plate rocks at Bare Mountain, Nevada—implications for extensional faulting. *Geol Geophys Charact Stud Yucca Mt Nev* 58:1–23
- Holland T, Powell R (1996a) Thermodynamics of order–disorder in minerals. I: symmetric formalism applied to minerals of fixed composition. *Am Miner* 81:1413–1424
- Holland T, Powell R (1996b) Thermodynamics of order–disorder in minerals. II: symmetric formalism applied to solid solutions. *Am Miner* 81:1425–1437
- Holland T, Powell R (1998) An internally consistent thermodynamic data set for phases of petrological interest. *J Metam Geol* 16:309–343
- Holland T, Baker J, Powell R (1998) Mixing properties and activity-composition and relationships of chlorites in the system MgO–FeO–Al<sub>2</sub>O<sub>3</sub>–SiO<sub>2</sub>–H<sub>2</sub>O. *Eur J Mineral* 10:395–406
- Inoue A, Meunier A, Patrier-Mas P, Rigault C, Beaufort D, Vieillard P (2009) Application of chemical geothermometry to low-temperature trioctahedral chlorites. *Clays Clay Miner* 57:371–382
- Inoue A, Kurokawa K, Hatta T (2010) Application of chlorite geothermometry to hydrothermal alteration in Toyoha geothermal system, southwestern Hokkaido, Japan. *Res Geol* 60:52–70
- Jowett E (1991) Fitting iron and magnesium into the hydrothermal chlorite geothermometer. *Program Abstr* 16:A62
- Karpov IK, Chudnenko KV, Kulik DA (1997) Modeling chemical mass transfer in geochemical processes: thermodynamic relations, conditions of equilibria, and numerical algorithms. *Am J Sci* 297:767–806
- Kranidiotis P, MacLean W (1987) Systematics of chlorite alteration at the Phelps Dodge massive sulfide deposit, Matagami, Quebec. *Econ Geol* 82:1898–1911
- Kulik DA, Wagner T, Dmytrieva SV, Kosakowski G, Hingerl FF, Chudnenko KV, Berner U (2013) GEM-Selektor geochemical modeling package: revised algorithm and GEMS3K numerical kernel for coupled simulation codes. *Comput Geosci* 17:1–24
- Lacroix B, Charpentier D, Buatier M, Vennemann T, Labaume P, Adatte T, Trave A, Dubois M (2012) Formation of chlorite



- during thrust fault reactivation. Record of fluid origin and P-T conditions in the Monte Perdido thrust fault (southern Pyrenees). *Contrib Mineral Petrol* 163:1083–1102
- Lanari P (2012) P-T mapping in metamorphic rocks. Applications to the Alps and the Himalaya. Ph.D. Thesis, University of Grenoble, p 544
- Lanari P, Guillot S, Schwartz S, Vidal O, Tricart P, Riel N, Beyssac O (2012) Diachronous evolution of the alpine continental subduction wedge: evidence from P-T estimates in the Briançonnais Zone houillère (France—Western Alps). *J Geodyn* 56–57:39–54
- Lanari P, Riel N, Guillot S, Vidal O, Schwartz S, Pêcher A, Hattori K (2013a) Deciphering high-pressure metamorphism in collisional context using microprobe-mapping methods: application to the Stak eclogitic massif (NW Himalaya). *Geology* 41:111–114
- Lanari P, Rolland Y, Schwartz S, Vidal O, Guillot S, Tricart P, Dumont T (2013b) P-T-t estimation of syn-kinematic strain in low-grade quartz-feldspar bearing rocks using thermodynamic modeling and  $^{40}\text{Ar}/^{39}\text{Ar}$  dating techniques: example of the Plan-de-Phasy shear zone unit (Briançonnais Zone, Western Alps). *Terra Nova*. doi:10.1111/ter.12079
- Lanari P, Vidal O, de Andrade V, Dubacq B, Lewin E, Grosch E, Schwartz S (2014) XMapTools: a MATLAB®-based program for electron microprobe X-ray image processing and geothermobarometry. *Comp Geosci* 62:227–240
- Le Hébel F, Vidal O, Kienast JR, Gapais D (2002) Les «Porphyroïdes» de Bretagne méridionale: une unité de HP-BT dans la chaîne Hercynienne. *CR Académie des Sciences, Géoscience* 334:205–211
- Malasoma A, Marroni M (2007) HP/LT metamorphism in the Volparone Breccia (Northern Corsica, France): evidence for involvement of the Europe/Corsica continental margin in the Alpine subduction zone. *J Metam Geol* 25:529–545
- Martin C, Debaille V, Lanari P, Goderist S, Vanhaecke F, Vidal O, Claeys P (2013) REE and Hf distribution among mineral phases in the CV-CK clan: a way to explain present-day Hf isotopic variations in chondrites. *Geochim Cosmochim Acta* 120:495–513
- Moazzen M (2004) Chlorite–chloritoid–garnet equilibria and geothermometry in the Sanandaj–Sirjan metamorphic belt, southern Iran. *Iran J Sci Technol* 28:1–14
- Mountain BW, Williams-Jones AE (1995) Mass transfer and the path of metasomatic reactions in mesothermal gold deposits: an example from Flambeau Lake, Ontario. *Econ Geol* 91:302–321
- Muñoz M, De Andrade V, Vidal O, Lewin E, Pascarelli S, Susini J (2006) Redox and speciation micromapping using dispersive X-ray absorption spectroscopy: application to iron in chlorite mineral of a metamorphic rock thin section. *Geochem Geophys Geosyst* 7:Q11020
- Muñoz M, Vidal O, Marcaillou C, Pascarelli O, Mathon O, Farges F (2013) Iron oxidation state in phyllosilicate single crystals using Fe-K pre-edge and XANES spectroscopy: effects of the linear polarization of the synchrotron X-ray beam. *Am Mineral* 98(7):1187–1197
- Parra T, Vidal O, Agard P (2002a) A thermodynamic model for Fe–Mg dioctahedral K white micas using data from phase-equilibrium experiments and natural pelitic assemblages. *Contrib Mineral Petrol* 143:706–732
- Parra T, Vidal O, Jolivet L (2002b) Relation between the intensity of deformation and retrogression in blueschist metapelites of Tinos Island (Greece) evidenced by chlorite–mica local equilibria. *Lithos* 63:41–66
- Percival S, Kodama H (1989) Sudoite from Cigar Lake, Saskatchewan. *Can Mineral* 27:633–641
- Plissart G, Femenias O, Maruntiu M, Diot H, Demaiffe D (2009) Mineralogy and geo- thermometry of grabbro-derived listveinites in the Tisovita-Iutu ophiolite, Southwestern Romania. *Can Mineral* 47:81–105
- Pourteau A, Sudo M, Candan O, Lanari P, Vidal O, Oberhänsli R (2013) Neotethys closure history of Anatolia: insights from  $^{40}\text{Ar}$ – $^{39}\text{Ar}$  geochronology and P-T estimation in high pressure metasedimentary rocks. *J Metam Geol* 31:585–606
- Powell R, Holland T (1993) On the formulation of simple mixing models for complex phases. *Am Miner* 78:1174–1180
- Powell R, Holland T (1999) Relating formulations of the thermodynamics of mineral solid solutions; activity modeling of pyroxenes, amphiboles, and micas. *Am Miner* 84:1–14
- Powell R, Holland TJB (2008) On thermobarometry. *J Metam Geol* 26:155–179
- Powell R, Holland TJB, Worley B (1998) Calculating phase diagrams involving solid solutions via non-linear equations, with examples using THERMOCALC. *J Metam Geol* 16:577–588
- Rimmelé G, Parra T, Goffé B, Oberhänsli R, Jolivet L, Candan O (2006) Exhumation paths of high-pressure–low-temperature metamorphic rocks from the Lycian nappes and the menderes massif (sw turkey): a multi-equilibrium approach. *J Petrol* 46:641–669
- Rolland Y, Carrio-Schaffhauser E, Sheppard S, Pêcher A, Esclauze L (2006) Metamorphic zoning and geodynamic evolution of an inverted crustal section (Karakorum margin, N Pakistan), evidence for two metamorphic events. *Intern J Earth Sci* 95:288–305
- Russo S, Cutrupia D, Di Bella M, Minutoli C (2006) High-pressure metamorphism in southern Calabria, Italy: the Cardeto chlorite–garnet metapelites. *Period Mineral* 75:23–42
- Saravanan CS, Mishra B, Jairam MS (2009) P-T conditions of mineralization in the Jonnagiri granitoid-hosted gold deposit, eastern Dharwar Craton, southern India: constraints from fluid inclusions and chlorite thermometry. *Ore Geol Rev* 36:333–349
- Schmidt D, Schmidt S, Mullis J, Ferreira Mähmann R, Frey M (1997) Very low grade metamorphism of the Taveyanne formation of western Switzerland. *Contrib Mineral Petrol* 129:385–403
- Schwartz S, Tricart P, Lardeaux JM, Guillot S, Vidal O (2009) Late tectonic and metamorphic evolution of the Piedmont accretionary wedge (Queyras Schistes lustrés, western Alps): evidences for tilting during Alpine collision. *GSA Bull* 121:502–518
- Serafimovski T, Dolenec T, Tasev G (2006) Actinolite–phengite–chlorite metasomatites from the Toranica Pb–Zn ore deposit in Macedonia. *Mater Geoenviron* 53:445–453
- Shinjoe H, Goto A, Kagitani M, Sakai C (2009) Ca–Al hydrous silicates in the chlorite-grade pelitic schists in Sanbagawa metamorphic belt and a petrogenetic analysis in the model mixed-volatile system. *J Mineral Petrol Sci* 104:263–275
- Tarantola A, Mullis J, Guillaume D, Dubessy J, de Capitani C, Adbelmoula M (2009) Oxidation of  $\text{CH}_4$  to  $\text{CO}_2$  and  $\text{H}_2\text{O}$  by chloritization of detrital biotite at 270 °C in the external part of the Central Alps, Switzerland. *Lithos* 112:497–510
- Theye T, Seidel E (1991) Petrology of low-grade high-pressure metapelites from the External Hellenides (Crete, Peloponnese). A case study with attention to sodic minerals. *Eur J Mineral* 3:343–366
- Theye T, Seidel E, Vidal O (1992) Carpholite, sudoite and chloritoid in low-grade high-pressure metapelites from Crete and the Peloponnese, Greece. *Eur J Mineral* 4:487–507
- Trotet F, Vidal O, Jolivet L (2001) Exhumation of Syros and Sifnos metamorphic rocks (Cyclades, Greece). New constraints on the P-T paths. *Eur J Mineral* 13:901–920
- Verlaguet A, Goffé B, Brunet F, Poinssot C, Vidal O, Findling N, Menut D (2011) Metamorphic veining and mass transfer in a chemically closed system: a case study in Alpine metabauxites (western Vanoise). *J Metam Geol* 29:275–300
- Vidal O, Parra T (2000) Exhumation paths of high-pressure metapelites obtained from local equilibria for chlorite–phengite assemblages. *Geol J* 35:139–161



- Vidal O, Goffé B, Theye T (1992) Experimental study of the stability of sudoite and magnesiocarpholite and calculation of a new petrogenetic grid for the system  $\text{FeO-MgO-Al}_2\text{O}_3\text{-SiO}_2\text{-H}_2\text{O}$ . *J Metam Geol* 10:603–614
- Vidal O, Goffé B, Bousquet R, Parra T (1999) Calibration and testing of an empirical chloritoid-chlorite Mg–Fe exchange thermometer and thermodynamic data for daphnite. *J Metam Geol* 17:25–39
- Vidal O, Parra T, Trotet F (2001) A thermodynamic model for Fe–Mg aluminous chlorite using data from phase equilibrium experiments and natural pelitic assemblages in the 100 to 600 °C, 1 to 25 kbar range. *Am J Sci* 301:557–592
- Vidal O, Parra T, Vieillard P (2005) Thermodynamic properties of the Tschermak solid solution in Fe-chlorite: application to natural examples and possible role of oxidation. *Am Miner* 90:347–358
- Vidal O, de Andrade V, Lewin E, Muñoz M, Parra T, Pascarelli S (2006) P-T-deformation- $\text{Fe}^{3+}/\text{Fe}^{2+}$  mapping at the thin section scale and comparison with XANES mapping: application to a garnet-bearing metapelite from the Sambagawa metamorphic belt (Japan). *J Metam Geol* 24:669–683
- Wagner T, Kulik DA, Hingerl F, Dmytrieva SV (2012) GEM-Selektor geochemical modeling package: TSolMod library and data interface for multicomponent phase models. *Can Mineral* 50:1173–1195
- Walshe JL (1986) A six-component chlorite solid solution model and the conditions of chlorite formation in hydrothermal and geothermal systems. *Econ Geol* 81:681–703
- Yamato P, Agard P, Burov E, Le Pourhiet L, Jolivet L, Tiberi C (2007) Burial and exhumation in a subduction wedge: mutual constraints from thermomechanical modeling and natural P-T-t data (Schistes Lustrés, western Alps). *J Geophys Res* 112:B07410
- Zang W, Fyfe W (1995) Chloritization of the hydrothermally altered bedrock at the Igarape Bahia gold deposit, Carajas, Brazil. *Mineral Deposita* 30:30–38